Università degli Studi di Firenze

Dipartimento di Ingegneria dell'Informazione (DINFO)

Corso di Dottorato in Ingegneria dell'Informazione

Curriculum: Electronics, Electromagnetics and Electrical Systems

Development and Validation of Novel Approaches for Real-Time Ultrasound Vector Velocity Measurements

Academic Discipline (SSD) ING-INF/01

Candidate
Stefano Rossi

Supervisor
Prof. Piero Tortoli

PhD Coordinator
Prof. Fabio Schoen

ciclo XXXIII, 2017/2020

Università degli Studi di Firenze,
Dipartimento di Ingegneria dell’Informazione (DINFO).

Thesis submitted in partial fulfillment of the requirements for the degree of
Doctor of Philosophy in Information Engineering.

October 2020

Contents

Chapter 1. Introduction

1.1 Objective

Medical echographic techniques exploit a form of mechanical energy, the ultrasound, characterized by vibrating particles within a medium, which does not involve harmful effects on biological tissues. The wide diffusion of modern ultrasound scanners is favored by their relatively low cost, compared to other medical imaging systems, and by their portability, which allows performing exams at the patient's bedside or in the operating room. The most known applications are fetal, musculoskeletal, and cardiovascular ultrasound. The latter ones are oriented to the investigation of morphological and functional characteristics of the circulatory system and have encouraged the development of methods capable of extrapolating detailed information of vascular mechanics and dynamics. For example, Doppler methods [1] focus on blood flow and tissue motion for the diagnosis and follow-up of cardiovascular diseases, which is today’s leading causes of death in the world [2], as shown in Fig. 1-1.

So far, several Doppler systems have been developed, each of them with its strengths and weaknesses. The first Doppler methods, which are still widely used in clinics, can reliably detect only one component (the axial one) of the motion. Therefore, to assess the motion velocity module, the

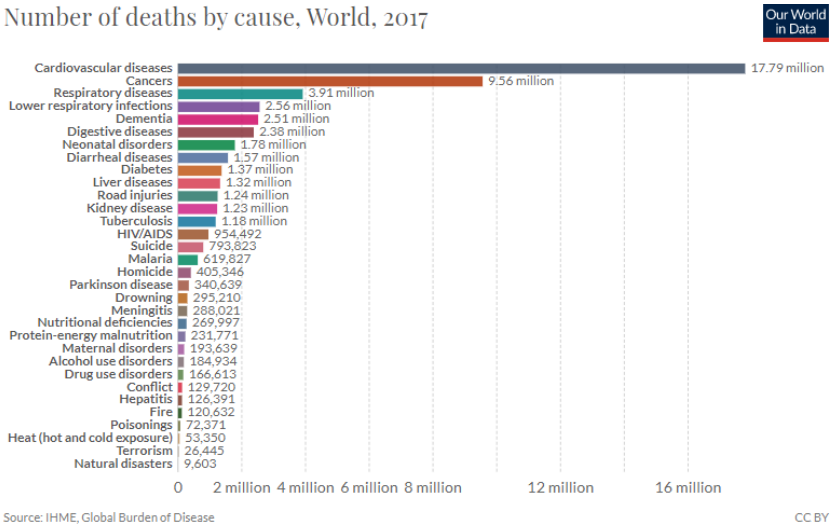

Fig. 1-1 Breakdown of global deaths in 2017 indexed by cause.

angle between the velocity under test and the ultrasound propagation direction must be known. Such angle is usually heuristically estimated by the operator. This leads to unavoidable measurement inaccuracies, which are particularly detrimental, e.g. in vessels' stenosis or bifurcations, where the flow can be turbulent. More advanced methods are needed to solve this problem by estimating the three components of the velocity vector.

The aim of this PhD project was to contribute to the development of novel real-time "vector Doppler" methods, by evaluating, in particular, their accuracy and computational load. Each development step was based on simulations and experimental tests. The former ones were based on Field II© [3], [4]and Simag [5], an ultrasound system simulator developed by the Microelectronics Systems Design Laboratory (MSDLab) of the University of Florence. The experiments were conducted by the ULtrasound Advaced Open Platform (ULA-OP 256, [6]), developed in the same MSDLab.

The work started with a thorough investigation of the recently proposed 2-D high frame rate (HFR) vector flow imaging (VFI) method based on the frequency domain for displacement estimation [7]. Three main issues were addressed: 1) the high blood velocity underestimation observed when examining vessels at great depths, 2) the high computational load, which hindered possible real-time implementations; 3) the lack of information about the third velocity component.

By means of simulations and experimental tests, it was found that the velocity underestimation at great depths is due to the progressive broadening of the transmitted beam on the elevation plane originated by the probe acoustic lens.

The computational cost of the 2-D VFI method has been significantly reduced by processing demodulated and down-sampled baseband (BB) data rather than radiofrequency (RF) data. Based on this novel approach, a preliminary real time version of the 2-D VFI method was implemented. Furthermore, it was found that the parallel computing features of graphic processing units (GPUs) are ideal for the implementation of this method. An expansion circuit board, which allocates GPU resources was thus designed and built for the ULA-OP 256 hardware. This new system architecture is currently under test and looks promising for a wide class of ultrasound processing methods.

Finally, a novel method for 3-D VFI was developed and tested both in simulation and experiments at different beam to flow angles. Specifically, it was based on the 2-D VFI, which was extended by an efficient estimation strategy to considerably limit the additional computational load.

The Thesis is organized as follows:

- **Chapter 2** illustrates the basics of ultrasonic wave propagation with focus on flow imaging methods.
- **Chapter 3** briefly introduces Simag and the ULA-OP 256.
- **Chapter 4** introduces the problem of the high underestimation at great depths for 2-D VFI and proposes possible solutions.
- **Chapter 5** presents a novel ultrasound 3-D vector Doppler technique together with simulation and experimental results.
- **Chapter 6** presents a first real-time implementation of 2-D VFI on the ULA-OP 256.
- **Chapter 7** gives an overview of the hardware developed to accommodate GPUs on the ULA-OP 256.
- **Chapter 8** concludes the thesis and gives future perspectives.

1.2 Contributions

Conference Proceedings

- **S. Rossi**, F. Fool, A. Ramalli and P. Tortoli, "**Experimental Validation of a New Method for 3-D Vector Flow Imaging in the Frequency Domain**" in 2020 IEEE International Ultrasonics Symposium (IUS), Las Vegas, NV, USA, Sep. 2020, pp. 1–3, doi: 10.1109/IUS46767.2020.9251341.
- **S. Rossi**, A. Ramalli, L. Francalanci and P. Tortoli, "**Influence of the Acoustic Lens on Vector Doppler Measurements Based on Plane Wave Transmission: a Simulation Study**" in 2020 IEEE International Ultrasonics Symposium (IUS), Las Vegas, NV, USA, Sep. 2020, pp. 1–3, doi: 10.1109/IUS46767.2020.9251427.
- **S. Rossi**, F. Acerbi, A. Dallai, F. Guidi, V. Meacci, A. Ramalli and P. Tortoli, "**Real-Time System for High Frame Rate Vector Flow Imaging**" in 2020 IEEE International Ultrasonics Symposium (IUS), Las Vegas, NV, USA, Sep. 2020, pp. 1–4, doi: 10.1109/IUS46767.2020.9251328.
- **S. Rossi**, A. Ramalli, S.Ricci, R. Matera, F. Guidi, E.Boni and P.Tortoli, "**Performance of Ultrasound Vector Velocity Measurement at Great Depths**," in 2019 IEEE International Ultrasonics Symposium (IUS), Glasgow, United Kingdom, Oct. 2019, pp. 368–371, doi: 10.1109/ULTSYM.2019.8925547.
- **S. Rossi**, M. Lenge, A. Dallai, A. Ramalli and E. Boni, "**Toward the Real Time Implementation of the 2-D Frequency-Domain Vector Doppler Method**," in Applications in Electronics Pervading Industry, Environment and Society, vol. 573, S. Saponara and A. De Gloria, Eds. Cham: Springer International Publishing, 2019, pp. 129–135. doi: 10.1007/978-3-030-11973-7_16
- R. Matera, V. Meacci, **S. Rossi**, D. Russo, S. Ricci and D. Lootcns, "**Smart Ultrasound Sensor for Non-Destructive Tests**," in 2018 New Generation of CAS (NGCAS), Valletta, Malta, Nov. 2018, pp. 29–32, doi: 10.1109/NGCAS.2018.8572207.

Journal paper

- **S. Rossi**, A. Ramalli, F. Fool, and P. Tortoli, “**High-Frame-Rate 3-D Vector Flow Imaging in the Frequency Domain**,” Applied Sciences, vol. 10, no. 15, p. 5365, Aug. 2020, doi: 10.3390/app10155365.
- **S. Rossi**, E. Boni, “**Embedded GPU Implementation for High-Performance Ultrasound Imaging**”, Electronics, vol. 10, n. 8, Art. n. 8, gen. 2021, doi: 10.3390/electronics10080884.
- **S. Rossi**, A. Ramalli and P. Tortoli, “**On the depth-dependent accuracy of plane-wave based vector velocity measurements with linear arrays**”, IEEE Transactions on Ultrasonics, Ferroelectrics, and Frequency Control, pag. 1–1, 2021, doi: 10.1109/TUFFC.2021.3076284.

Chapter 2. Ultrasound Basics

This chapter briefly describes the fundamentals of ultrasound physics. It also introduces the blood flow ultrasound imaging methods of interest for this thesis.

2.1 Ultrasound Overview

"Ultrasounds" identify the pressure waves, i.e. mechanical vibrations in a medium, characterized by a frequency higher than 20 kHz, i.e. the higher limit of the audible spectra. The longitudinal propagation of pressure waves leads to the oscillation of the particles around their equilibrium position, propagating their movements to the neighboring ones, as shown schematically in Fig. 2-1. This implies a compression (dark red) and rarefaction (light pink) of these particles, according to the direction of the propagation of the wave.

Analytically the linear wave propagation (i.e. along only one direction), can be defined as:

$$\frac{\partial^2 T}{\partial z^2} = \frac{\rho}{\beta} \cdot \frac{\partial^2 T}{\partial t^2} \tag{2.1}$$

where T [N/m^2] represents the stress while ρ [kg/m^3] and β [kg/(m s^2)] are the volumetric density and the elastic constant of the medium, respectively. The generic solution is the well know plane wave function:

$$T(z,t) = T_0 \cdot e^{j(2\pi f t \pm kz)} \tag{2.2}$$

where T_0 [N/m^2] is the peak of pressure module, f [Hz] the oscillation frequency and k [1/m] is the elasticity of the medium:

$$k = \frac{2\pi f}{c} = \frac{2\pi}{\lambda} \tag{2.3}$$

where λ [m] is the wavelength, i.e. the distance between two consecutive crests of the wave, while c is the propagation speed of the wave through the medium, which is defined as:

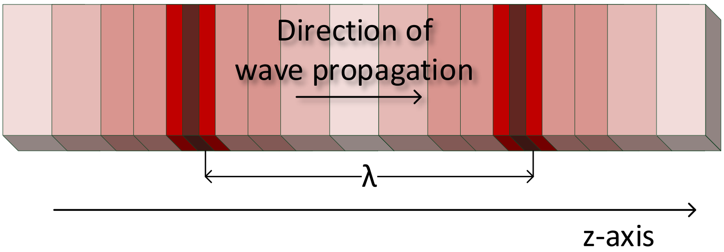

Fig. 2-1 A longitudinal wave propagating in a linear homogeneous medium, where λ is the wavelength.

$$c = \sqrt{\beta/\rho} \qquad (2.4)$$

The latter highlights that the propagation speed is strictly related to the chemical and physical nature of the material. For this reason, the aggregation property of materials, or the molecular and atomic bounds have a heavy impact on such effect. The acoustic impedance Z [1 Rayl = 1 kg/(m^2 s)], which characterizes the resistance that a medium opposes against the propagation of the pressure wave, is defined as:

$$Z = \rho \cdot c \qquad (2.5)$$

As a reference, Table 2.I summarizes the acoustic parameters of the main biological media.

TABLE 2.I

ACOUSTIC PARAMETERS OF BIOLOGICAL MEDIA

Medium	**Sound speed**	**Volumetric density**	**Attenuation coefficient**	**Acoustic impedance**
	***c* [m/s]**	***ρ* [kg/m^3]**	**α_{AdB} [dB/(cm MHz)]**	***Z* [MRayl]**
Air	330	1.2	-	0.0004
Blood	1584	1060	0.2	1.68
Bone (cortical)	3476	1975	6.9	7.38
Bone (trabecular)	1886	1055	9.94	1.45
Brain	1560	1040	0.6	1.62
Breast	1510	1020	0.75	1.54
Cardiac	1576	1060	0.52	1.67
Connective Tissue	1613	1120	1.57	1.81
Cornea	1585	1076	-	1.71
Dentin	3800	2900	80	8.0
Enamel	5700	2100	120	16.5
Fat	1478	950	0.48	1.40
Liver	1595	1060	0.5	1.69
Marrow	1435	-	0.5	-
Muscle	1547	1050	1.09	1.62
Tendon	1670	1100	4.7	1.84
Soft tissue	1561	1043	0.54	1.63
Water	1480	1000	0.0022	1.48

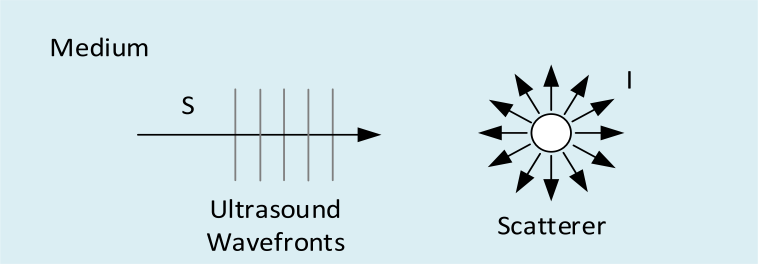

Fig. 2-2 The scattering phenomenon: the target scatterer, on the right, spreads the incident energy in all directions.

The propagation of an ultrasonic wave obeys to the same phenomena of any other wave field propagating in a heterogeneous medium, i.e. scattering, reflection, refraction, and attenuation. When an ultrasound wave meets an obstacle whose size is smaller or comparable to the wavelength, it 'bends' around the obstacle's corner, obeying to the so-called Rayleigh scattering (Fig. 2-2). Here, the incident energy (S) is partially transferred to the particle and "isotropically" spread (I) in all directions. The scattering cross section (σ) is defined by the ratio:

$$\sigma = S/I \tag{2.6}$$

In the ultrasound imaging field this parameter is of major importance because it is closely related to the amount of echo signal power available to the ultrasound system.

On the contrary, if the wavelength of the ultrasound wave is larger than the interface roughness, refraction and reflection occur. Referring to Fig. 2-3, when a wave reaches, with an incident angle ϑ_i, the separation surface between two media (A and B), whose acoustic impedances are Z_A and Z_B, a part of the energy is transmitted (refracted) to the medium B, while the remaining is reflected back to the propagation medium. The reflection (ϑ_r) and transmission (ϑ_t) angles are related with ϑ_i through the Snell's law:

$$\frac{\sin\vartheta_i}{c_A} = \frac{\sin\vartheta_t}{c_B} \tag{2.7}$$

$$\vartheta_i = \vartheta_r \tag{2.8}$$

where c_A and c_B are the wave speed for the two media.

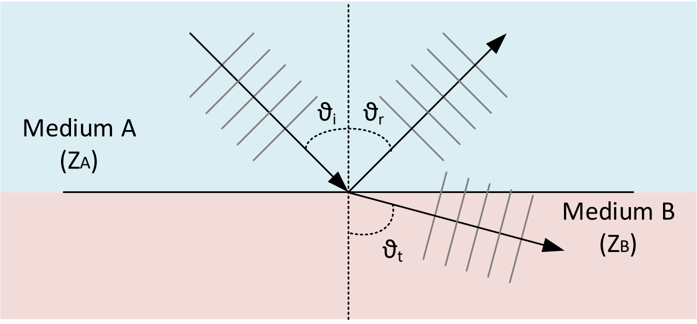

Fig. 2-3 Wave propagation through medium discontinuities. ϑ_i, ϑ_r *and* ϑ_t *are the incidence, reflection and transmission angles, respectively.*

The reflected and transmitted energies are respectively proportional to the following coefficients:

$$R = \left(\frac{Z_B \cos\vartheta_i - Z_A \cos\vartheta_t}{Z_B \cos\vartheta_i + Z_A \cos\vartheta_t}\right)^2 \tag{2.9}$$

$$T = 1 - R = \frac{4\, Z_A\, Z_B \cos\vartheta_i \cos\vartheta_t}{(Z_B \cos\vartheta_i + Z_A \cos\vartheta_t)^2} \tag{2.10}$$

Finally, even if an ultrasound wave that propagates in a non-ideal medium does not encounter obstacles or discontinuities, it is still subject to the attenuation phenomenon. As already pointed out, the propagation of ultrasound in a medium occurs by the movement of the particles, by compression, expansion and sliding. This phenomenon leads to a dissipation of heat energy (absorption). It is referred to attenuation even when there is a loss of kinetic energy due to scatterers or phenomena of refraction and reflection. Analytically the signal intensity I [dB/(cm MHz] decrease exponentially along the propagation direction. For example, if the ultrasound wave propagates along z-axis it results:

$$I = I_0 e^{-2\alpha_A z} \tag{2.11}$$

where I_0 is the initial intensity, and α_A [W/m^2] is the attenuation coefficient, usually related in dB/m:

$$\alpha_{AdB} = \frac{10}{W} \log \frac{I}{I_0} \tag{2.12}$$

with W [m] is the tissue width or thickness. Table 2.I reports the attenuation coefficients of the main biological media.

2.1.1 Transducers

The most common ultrasonic probes are constituted of piezoelectric transducers. This material is composed of electrical dipoles orderly distributed, which can be altered by applying a mechanical stress or an electric signal. The simplified structure of a single transducer could be compared to a capacitor, as shown in Fig. 2-4, with the piezoelectric material interfaced between two electrical terminals. When a pressure wave hits the piezoelectric crystal, contraction and traction movements cause positive and negative charges on the transducer terminals. This is called the direct piezoelectric effect and is exploited in the ultrasound reception phase. Instead, the reverse piezoelectric effect is used in transmission. Here a voltage is applied to the terminals, which changes the distribution of dipoles, inducing mechanical shortening and elongation.

Analytically, the phenomenon is described as:

$$\begin{cases} D = dT + \varepsilon^T E \\ S = s^E T + d^T E \end{cases} \tag{2.13}$$

The two equations define the direct and inverse effects, respectively. D and E are the electrical displacement and the electric field; S and T are the mechanical strain and mechanical stress; ε^T is the dielectric permittivity under a zero or constant stress; s^E is the compliance under a zero or

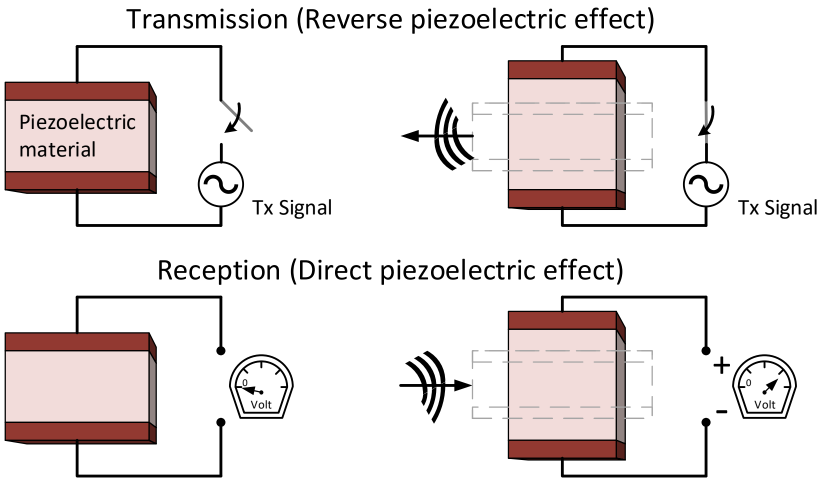

Fig. 2-4 Direct and indirect piezoelectric effects: representation of the ultrasound transmission and reception phases.

constant electrical field; d and d^T are the matrices for the direct and the reverse piezoelectric effect.

In general a transducer is characterized by the central resonance frequency f_0, which depends by the speed of sound and thickness of the piezoelectric crystal, and by the bandwidth B_W, which is defined as the frequency range around f_0 where the transfer function of the probe is greater to -3dB of its peak. A typical quality parameter of the probes is the "Q-Factor", defined as:

$$Q = \frac{f_0}{B_W} \tag{2.14}$$

Fig. 2-5 shows a schematic view of the main parts of a single crystal piezoelectric probe. The previously described structure, composed by a piezoelectric crystal between two electrodes, is anchored to a complex system formed by absorbing materials (backing layer) on one side, and by a coupling surface (matching layer) on the other side. This design is necessary to solve two main problems. Primarily, the great difference between the acoustic impedances that characterize the sensor and the biological tissue implies that, without any interface, there would be total reflection of the transmitted signal. Hence, the matching layer is designed to have an intermediate impedance and to optimize the transmission of ultrasounds. The second issue is related to the resonance frequency of the piezoelectric crystal:

$$f_{res} = \frac{c_{piezo}}{2A} \tag{2.15}$$

where c_{piezo} and A are the sound propagation speed in the piezoelectric material and the stiffness of the crystal, respectively. The backing layer is

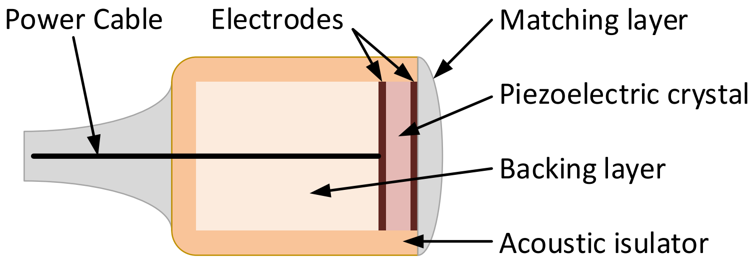

Fig. 2-5 Diagram of a basic mono-element ultrasound transducer design.

an absorbent material, placed on the opposite side of the crystal with respect the patient, which attenuates the multiple undesired reflections that propagate inside the transducer. These oscillations (ringing) have a negative impact on the imaging quality and resolution.

In the medical field, the most commonly used probes include several transducers, also called elements, which form an array and are arranged according to specific layouts: linear, convex, and phased. For example, in linear arrays, as shown in Fig. 2-6, the elements are parallel to each other and linearly spaced by a constant distance, referred to as "pitch". The structure is bounded by a backing base and, on the opposite side, by a matching layer and a cylindrical lens for elevation focusing. Although the use of array probes complicates the design of the ultrasound system, it is very convenient since the individual electronic control of each element allows focusing and steering the ultrasound beam at different positions and directions. Typically, this is done by controlling both transmission delays and amplitudes (also called apodization) of the signals transmitted by each individual element. This versatility is even more exploited in reception, through the so-called dynamic beamforming. It dynamically adapts both focusing delays and apodization weightings at each depth and coherently

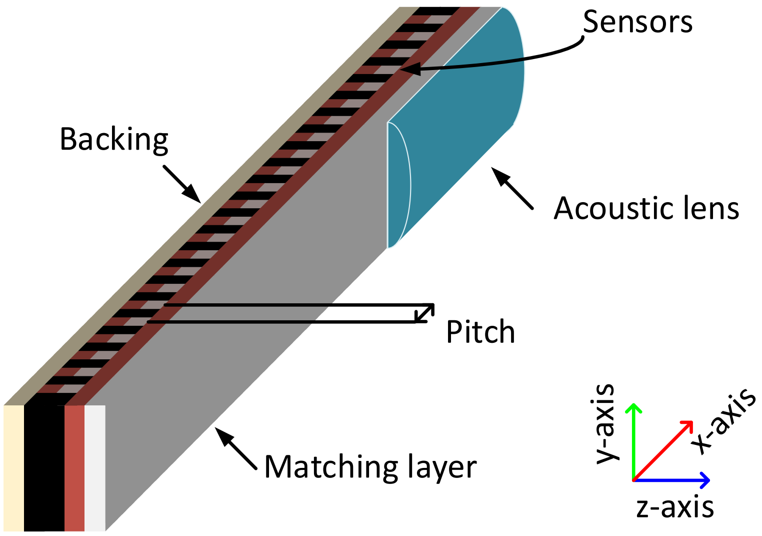

Fig. 2-6 Isometric sketch of a basic linear array probe.

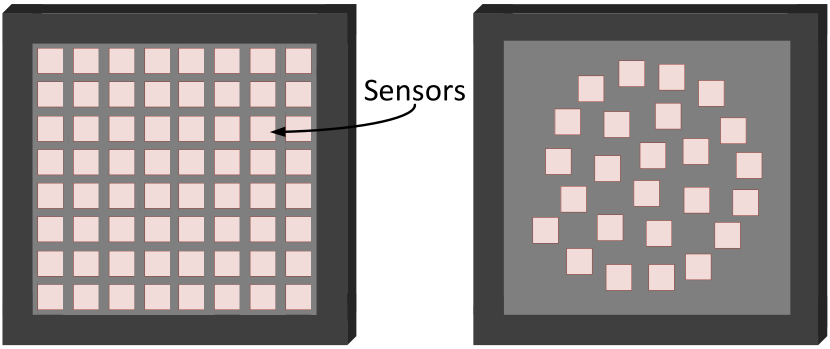

Fig. 2-7 Sensors distribution examples of a gridded 2-D array probe (left side) and a spiral (right side) ones.

recombines the echoes received by each element thus improving resolution and directivity.

More recently, technological developments on both system and probe sides pushed the development of volumetric (or three-dimensional, 3-D) imaging. Indeed, the increased number of independent channels of the system and the introduction of application specific integrated circuits (ASICs) inside the probe allow controlling 2-D array probes consisting of thousands of elements displaced on a 2-D matrix layout. Moreover, nowadays, sparse 2-D arrays [8] have been proposed to reduce cost and complexity of 3-D ultrasound systems based on random or spiral layouts, as shown in Fig. 2-7.

2.1.2 Pulsed Wave Imaging Systems

Ultrasound scanners are based on pulsed wave transmissions, i.e. on the transmission short ultrasound signals (burst). The time interval between two consecutive transmission events is defined as pulse repetition interval (PRI), which is the inverse of the pulse repetition frequency (PRF). After a transmission event, the ultrasound wave propagates in the medium before being backscattered to the transducer by any change of acoustic impedance. Given the propagation speed (c) of the medium and measuring the time delay (Δt) between transmission and reception of the echo, it is thus possible to compute the distance of the scatterer/interface as:

$$d = \frac{\mathrm{c}\,\Delta t}{2} \tag{2.16}$$

The non-ambiguous range of depths $[d_{min}: d_{MAX}]$ that can be investigated depends on the duration of the transmission burst *D*, the PRF, ant the propagation speed:

$$d_{min} = c \cdot D \tag{2.17}$$

$$d_{MAX} = \frac{c}{2 \cdot PRF} \tag{2.18}$$

Depending on the application, received signals can be gated to process data referring either to a single specific depth of interest (single gate) or to several depths within the non-ambiguous range (multigate), see Fig. 2-8.

The main blocks of a common ultrasound scanner based on pulsed wave transmission are shown in Fig. 2-9. A (optional) multiplexer or a T/R switch connects the transducers with both the transmission and reception chain. It ensures fast recovery times to quickly enable the receiver after the end of each transmission event. It is driven by the control unit, which also manages every operation during the reception phase. Typically, tri-level signal generators are employed in transmission, allowing the transmission of high voltage signals (up to V_{HV} = 100 V). In practice, transmission bursts consist in pulse width modulated waves with only three possible output values ($-V_{HV}$, 0, V_{HV}). In reception, the radio frequency backscattered signals are amplified by low noise amplifiers (LNA), which allow limiting the degradation of the signal-to-noise ratio and introducing low harmonic

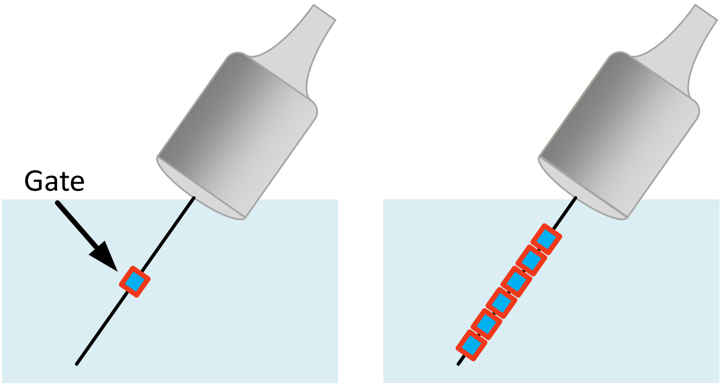

Fig. 2-8 Single gate (left) and multigate (right) acquisitions.

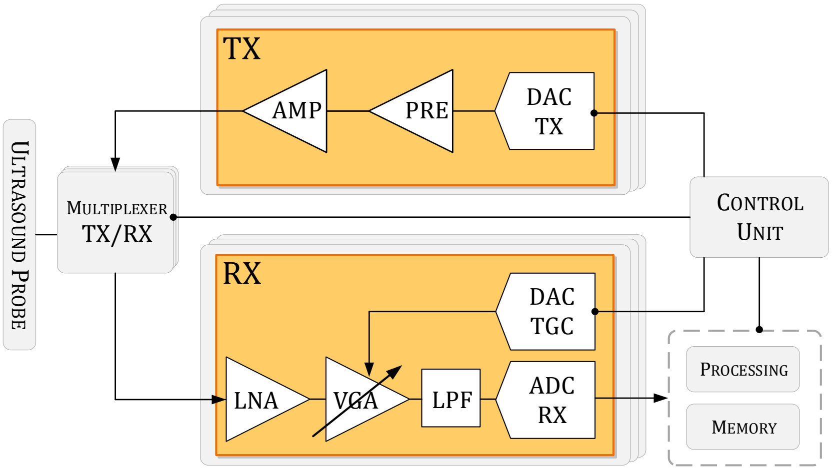

Fig. 2-9 :Block-diagram of the main of a multiplexed ultrasound system.

distortion. The amplification chain also includes variable gain (VGA) amplifiers piloted by the control unit, through the TGC DAC, to dynamically compensate for the depth dependent attenuation and low pass filters to mitigate the high frequency signal components. Finally, an analog to digital converter (ADC) digitalize the amplified and filtered echoes. The control unit also times data storage and signal processing such as filtering, demodulation and beamforming.

Plane Wave Imaging

The high frame rate (HFR) imaging techniques have become increasingly important in the ultrasound imaging field. Many 2-D and 3-D imaging applications are achievable by plane wave (PW) transmission techniques. The idea behind it is to maximize the output frame-rate, reducing the number of transmissions required to reconstruct an image. Unlike transmission methods based on focused beams (FBs), which sequentially scan a region of interest line by line, the PW technique, by transmitting defocused wide beams, allows reconstructing an image after each single transmission event, reaching frame rates as high as the PRF. This feature allows examining very fast phenomena, and makes this imaging method useful in applications such as elastography and flow ultrasound imaging [9].

Unsteered PWs, as wide as the aperture of the transmitting array, can be transmitted by simultaneously exciting all the transducer elements of the probe. They allow maximizing the frame-rate. However, this transmission strategy involves a reduction of the pressure amplitudes with respect to FBs and consequently a reduction of the signal to noise ratio (SNR) and of the penetration depth. Also, images suffer from an overall image quality degradation in terms of contrast and resolution. To overcome these problems compounding techniques were introduced. They consist in the transmission of several plane waves, steered along different direction, and in the coherent compound of the reconstructed images. The frame rate necessarily linearly decreases with the number of the transmission events, but SNR, spatial resolution, contrast and penetration depth increase.

2.2 Flow Imaging

Multigate Spectral Doppler

The multigate spectral Doppler (MSD) technique [10]–[12] allows estimating the blood flow speed at different depths along the same line of interest, thus reconstructing also the spatial distribution of the different speeds involved in blood flow. This technique requires that the echo signal received is previously sampled and demodulated. Repeating the operation on a given number of successive PRIs results in a time domain matrix. The directions identified by the dimensions of this matrix are generally indicated as fast time (samples relative to the same PRI but at different depths) and slow time (samples relative to different PRI but at the same depth of investigation). The different Doppler profiles can be obtained by a Fourier Transform (FT) applied along the slow time direction for each investigated depth and represented as shown in Fig. 2-10. It shows the spectral profiles detected for a parabolic flow where the vertical axis corresponds to depth and the horizontal axis to the Doppler frequency, while power spectral densities are color-coded according to the colormap on the right. Since MSD provides good depth and time resolution, it is extremely useful for the analysis of flow profiles within the vessels and during the different phases of the cardiac cycle.

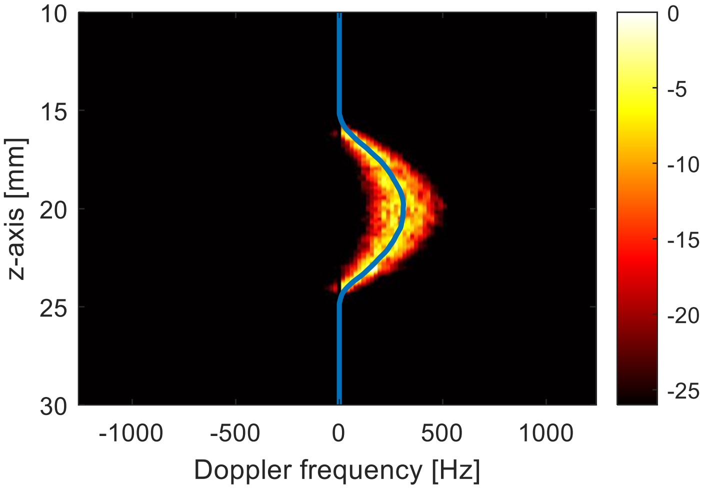

Fig. 2-10 :Example of multigate spectral Doppler imaging of parabolic flow profile. Power spectral densities are color-coded in dB.

Vector Doppler

The MSD detects only the axial velocity component (i.e. along the ultrasound propagation direction). This represent a minor issue when the flow direction can be assessed heuristically. On the other hand, when the flow assumes complex patterns, i.e. in the presence of curves, bifurcations or stenoses, the manual setting of the direction of the angle is not straightforward or is not possible at all thus bringing to high errors on the estimation of the flow velocity module. Another limit of MSD is that it does not provide 2-D or 3-D maps of flow distribution. Several techniques [13], [14] have therefore been proposed that automatically evaluate the module and angle (i.e. vector) of the flow and extend the measurement in multiple dimensions. The multi-beam approach trigonometrically combines multiple Doppler measurements, obtained from different transducers or apertures, to estimate all the velocity components [15]–[17], while other techniques exploited the spectral broadening to directly evaluate the transverse velocity component [18]–[20]. Other approaches reconstruct maps of velocity vectors [21] as those based on speckle tracking [22], [23] or those based on transverse oscillations [24]–[26]. Moreover, methods based on PW transmission were introduced such as those that exploit two transmissions with opposite steering angles [27],

[28] and those that obtain vector maps through operations based on 2-D cross-correlation [29]. Our group recently proposed a computationally efficient Vector Flow Imaging (VFI) method that estimates the displacements between consecutive radiofrequency (RF) frames by calculating the corresponding phase shifts in the frequency domain [6], [23]. This method, thoroughly investigated for this PhD project, will be detailed in the following paragraph.

2.3 2-D Vector Flow Imaging in the Frequency Domain

The VFI method is based on the transmission of PWs by a linear array probe and on the reconstruction of RF frames at high frame rate (HFR). Conversely from the methods proposed by other groups [28], [30], this 2-D VFI method does not use coherent compounding in reception. This implies that each velocity estimate is obtained by only two consecutive PW transmissions. Moreover, the computational load of this approach was shown to be 56 times lower than the conventional 2-D cross-correlation approach [10], while providing comparable flow estimates.

The main processing steps of the 2-D VFI method [7] are sketched in block diagram in Fig. 2-11. Each beamformed RF frame is preliminary clutter filtered, by a high pass filter, and then subdivided into partially overlapped rectangles (kernels) of $M_B \times N_B$ pixels uniformly distributed over the entire frame. To limit deleterious edge effects each kernel is weighted with a Hann's window. Let's define s_{mn} and $\tilde{s}_{mn}$ two kernels, located on the same position (*m*,*n*) on two consecutive frames, which were

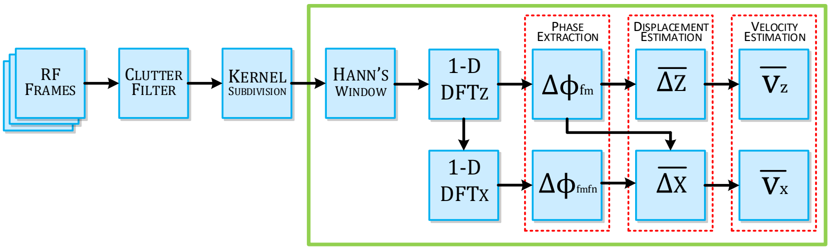

Fig. 2-11 Block diagram of the efficient 2-D VFI method. The green rectangular block describes the processing steps required to estimate the two velocity components for each kernel.

obtained at time t and t'= t + τ, respectively. If the scatterers inside such kernels cover a relatively short distance during the interval τ , $\tilde{s}_{mn}$ can be considered as a 2-D shifted version of s_{mn}. Hence, the Δz and Δx displacements can be computed from a 1-D discrete Fourier transform (DFT) for the z direction and a 2-D DFT for the x direction, as follows:

$$\Delta_{zf_m} = \frac{M_B}{2\pi f_m} \Delta\phi_{f_m} \tag{2.19}$$

$$\Delta_{zf_m f_n} = \frac{N_B}{2\pi f_n} \left(\Delta\phi_{f_m f_n} - \Delta\phi_{f_m}\right) \tag{2.20}$$

where f_m and f_n are the spatial frequencies in the z and x directions, respectively, while $\Delta\phi_{f_m}$ and $\Delta\phi_{f_m f_n}$ are the phase shifts in the frequency domain. In this work, according to [7], displacements were estimated at multiple frequencies to improve the robustness of estimates. Hence, n_{fz}= 3 frequencies were uniformly distributed on a 20% bandwidth around the transmission frequency *f₀*, while n_{fx} = 10 frequencies were distributed on negative and positive spatial frequencies in a bandwidth equal to 5% to 20% of the spatial sampling frequency (1/pitch).

Then, the displacements were averaged as follows:

$$\overline{\Delta z} = \frac{1}{n_{fz} N_B} \sum_{n=1}^{N_B} \sum_{m=1}^{n_{fz}} \frac{M_B}{2\pi f_m} \Delta\phi_{f_m n} \tag{2.21}$$

$$\overline{\Delta x} = \frac{1}{n_{fx} n_{fz}} \sum_{n=1}^{n_{fx}} \sum_{m=1}^{n_{fz}} \frac{N_B}{2\pi f_n} \left(\Delta\phi_{f_m f_n} - \Delta\phi_{f_m n}\right) \tag{2.22}$$

Finally, the velocity components were given by

$$\overline{v_z} = \overline{\Delta z}\, \delta z / \tau \qquad \overline{v_x} = \overline{\Delta x}\, \delta x / \tau \tag{2.23}$$

Although, as stated above, the proposed approach is highly computational load efficient, its implementation for real-time execution on the ULA-OP 256 is still critical due to the amount of data to be managed and processed. Hence, in this work, it is proposed to further reduce the computational load by processing demodulated and down-sampled baseband (BB) data, thus allowing a real-time implementation.

Chapter 3. Materials

The chapter provides an overview of the materials used for simulations, experiments and developments.

3.1 Simulation Tools: Simag & Field II

Simag is a software developed by the MSDLab, which provides an intuitive graphical user interface, for the simulation of ultrasound systems. It was conceived for research and didactic purposes [5], thus it guarantees high degrees of freedom in terms of available configurations. The user can set:

- the characteristics of the simulated medium: sound propagation speed, average attenuation, and frequency dependent attenuation;
- the transducer: type, number of elements, active elements layout, acoustic lens, pulse response, and bandwidth;
- the features of the system: sampling frequency in both transmission and reception, delay and apodization quantization levels;
- the transmission and reception strategy: the excitation signal, the focal depth, the apodization, the beamforming scheme in reception;

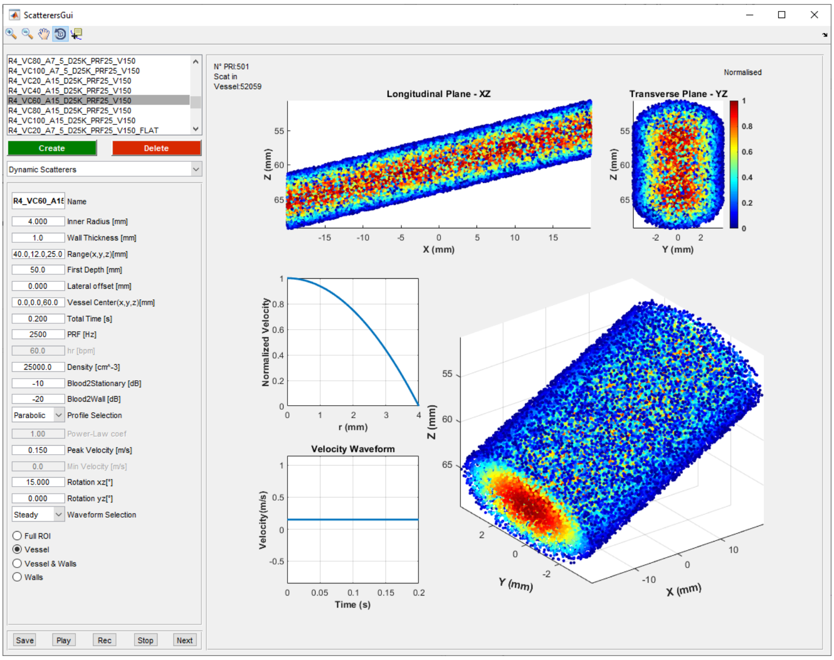

R4_VC80_A7_5_D25K_PRF25_V150
R4_VC100_A7_5_D25K_PRF25_V150
R4_VC20_A15_D25K_PRF25_V150
R4_VC40_A15_D25K_PRF25_V150
R4_VC60_A15_D25K_PRF25_V150
R4_VC80_A15_D25K_PRF25_V150
R4_VC100_A15_D25K_PRF25_V150
R4_VC20_A7_5_D25K_PRF25_V150_FLAT

Dynamic Scatterers

R4_VC60_A15 Name
4.000 Inner Radius [mm]
1.0 Wall Thickness [mm]
40.0,12.0,25.0 Range(x,y,z)[mm]
50.0 First Depth [mm]
0.000 Lateral offset [mm]
0.0,0.0,60.0 Vessel Center(x,y,z)[mm]
0.200 Total Time [s]
2500 PRF [Hz]
60.0 hr [bpm]
25000.0 Density [cm^-3]
-10 Blood2Stationary [dB]
-20 Blood2Wall [dB]
Parabolic Profile Selection
1.00 Power-Law coef
0.150 Peak Velocity [m/s]
0.0 Min Velocity [m/s]
15.000 Rotation xz[°]
0.000 Rotation yz[°]
Steady Waveform Selection

○ Full ROI
● Vessel
○ Vessel & Walls
○ Walls

Fig. 3-1 Simag: setting interface for numerical phantoms. This example shows the settings for a 4-mm radius, 40-mm long phantom, placed at 60 mm with a rotation angle of 15° on the xz-plane. The flow profile was set to parabolic.

- the numerical phantom: static/dynamic position of the point-scatterers, scattering amplitude, density, spatial and temporal velocity profile, as shown in Fig. 3-1.

According to the above settings, the software allows the simulation of B-mode images and Doppler profiles of numerical phantoms, acoustic beam profiles in transmission (one-way field) and in reception (two-way field), together with the related propagation of the acoustic wave. Also, the software shows the echo signals received by each single transducer of the probe at each stage of the reception chain.

The core of Simag is Field II© [3], [4] which is the international reference for the simulation of linear ultrasound propagation. This software is an application package composed of several functions for ultrasound simulation, implemented in C and provided with Matlab® (The MathWorks Inc., Natick, MA, USA) functions. The latter are used as interface between Matlab and the C code. In such a way the advantages in terms of computation speed of C codes and the versatility of a development tool are both exploited.

Fig. 3-2 The ultrasound advanced open platform ULA-OP 256 connected to a linear array.

In Simag, the package Field II is only exploited to simulate the ultrasound propagation, each system parameter and setting, e.g. beamforming or signal generation, is directly and individually computed by the mathematical modules of Simag.

3.2 ULA-OP 256

The Ultrasound Advanced Open Platform 256 (ULA-OP 256) is a compact open system developed by the MSDLab for research purposes. The system was designed to control up to 256 independent transmission and reception channels, allowing full control of both linear and 2-D probes. ULA-OP 256 supports both real-time modes and allows the acquisition of raw and processed data at any point of the reception chain.

The architecture of the ultrasound scanner sketched in Fig. 3-3, is composed of 8 Front End boards (FEs), each managing 32 channels, a Master Control board (MC) and a power supply board, which are interconnected through the Back-Plane (BKP) board which also houses the probe connector. Table 3.I summarizes the main features of the ultrasound scanner. The architecture allows a modular approach to operate with a limited number of FEs, which is commonly used with specific probes with

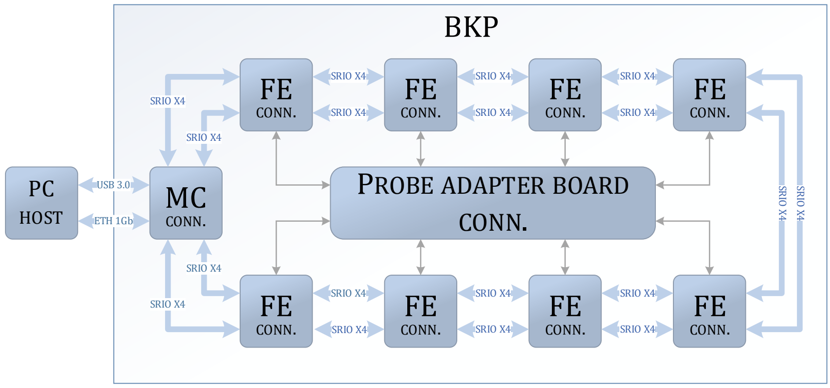

Fig. 3-3 Block diagram of the general architecture of the ULA-OP 256. Eight front-end (FE) boards communicate with the master control (MC) board in a ring-network. Each FE board manage 32 channels connected to the probe, through an adapter board.

TABLE 3.I

ULA-OP 256 MAIN FEATURES

General Features	Open platform 32 to 256 independent Tx/Rx channels Size: 34 x 30 x 26 cm
Transmitters	32 to 256 arbitrary waveform generators based on a 625 Mb/s sigma-delta bitstream Max output voltages: 200 Vpp Frequency: 1 to 20 MHz
Receiver	Bandwidth: 1 to 30 MHz Analog gain: 2 – 54 dB with 0 to 40 dB programmable TGC 12-bit @ 78.125 MHz ADCs
Beamformer	Programmable apodization and delays (dynamic focusing delay and sum beamformer, with resolution of 1/16 of the sampling period)
Processing Modules	Coherent demodulation, band-pass filtering, downsampling, B-mode, multi-gate spectral Doppler, vector Doppler, etc (with the possibility to create new custom modules by the end user)
Storage Capabilities	Up to 144 GB for RF (pre- or post-beamformed) and baseband data

fewer elements (for example, 4 FEs are enough to control 128-element probes, while only 6 FEs are required to manage 192-element arrays).

The FEs integrate the electronics needed to manage the transmission (Tx), the reception (Rx), and the real-time processing of 32 channels. The transmission waveform is generated by an FPGA from the ARRIA V GX Family (Altera, San Jose, CA, USA), which is programmed to generate sigma-delta modulated bitstreams, at 625-Mb/s rate, in the low-voltage differential signaling (LVDS) format. These bitstreams are sent to a daughterboard, where are converted to an analog waveform by a low-pass filter and a power amplified. Still on the FEs, the received echo signals are amplified, time-gain compensated, and digitized at 78.125 MHz with 12-bit resolution by four 8-channel circuits (AFE5807, Texas Instruments). The same, above-mentioned, FPGA also performs the first stage of the delay and sum beamforming for 32 channels.

Each FE also hosts two 8-core DSPs (TMS320C6678, Texas Instruments, Austin, TX, USA), running at 1.2 GHz, and 8 GB of DDR3 memory. These are in charge of real-time processing operations, such as coherent demodulation, filtering and compounding. Each FE board has four SerialRapidIO (SRIO) interfaces that are interconnected in a ring path on the BKP, achieving with a full duplex bandwidth of 10-GB/s.

The MC board hosts a multicore DSP (TMS320C6678) and one FPGA from the family (Altera, Cyclone V). The DSP performs the second-stage of the beamforming, hence it collects and sums the partially beamformed data processed on the FEs. Moreover, the DSP processes the beamformed data according to specific processing modes, such as B-mode, multigate spectral Doppler or vector Doppler Furthermore, it manages the interaction between the system and a host PC by means of a USB 3.0 SuperSpeed connection and Ethernet (ETH) protocol.

The ULA-OP 256 is managed by a modular and highly configurable software, running on the host PC, which initializes the hardware upon startup, and, through a user-friendly interface, displays in real-time the results of the ultrasound data processing. The settings of each transmission, reception and processing resources are programmed by text configuration files. Through the software graphical interface, the user can change, on the fly, several processing parameters, collected in specific popup control panels, and immediately observe the effects. Moreover, in order to perform offline processing, it is possible to download and store locally, the data before each processing phase (demodulation, beamforming, etc.).

Chapter 4. Blood Velocity Estimation at Great Depths

High frame rate vector Doppler methods exploit the transmission of plane waves to estimate blood velocities over wide 2-D regions. The estimation accuracy typically deteriorates at greater depths. This chapter evaluates the reasons of such underestimation and demonstrates that they are mainly due to the divergence of the acoustic beam produced by the probe acoustic lens.

The activity reported in this chapter resulted in the following publications:

***S. Rossi**, A. Ramalli, L. Francalanci and P. Tortoli, "**Influence of the Acoustic Lens on Vector Doppler Measurements Based on Plane Wave Transmission: a Simulation Study**" in 2020 IEEE International Ultrasonics Symposium (IUS), Las Vegas, NV, USA, Sep. 2020, pp. 1–3, doi: 10.1109/IUS46767.2020.9251427.*

***S. Rossi**, A. Ramalli, S.Ricci, R. Matera, F. Guidi, E.Boni and P.Tortoli, "**Performance of Ultrasound Vector Velocity Measurement at Great Depths**," in 2019 IEEE International Ultrasonics Symposium (IUS), Glasgow, United Kingdom, Oct. 2019, pp. 368–371, doi: 10.1109/ULTSYM.2019.8925547.*

***S. Rossi**, A. Ramalli and P. Tortoli, "**On the depth-dependent accuracy of plane-wave based vector velocity measurements with linear arrays**", IEEE Transactions on Ultrasonics, Ferroelectrics, and Frequency Control, pag. 1–1, 2021, doi: 10.1109/TUFFC.2021.3076284.*

4.1 Introduction

Vector Doppler methods based on the transmission of plane waves (PWs) from linear arrays are increasingly used thanks to their capability of estimating detailed blood flow maps over wide regions of interest. New methods are typically demonstrated in applications involving the analysis of limited range of depths, such as for the carotid artery. Their performance for the investigation of deep vessels such as the aorta, is typically under-explored. Only in the case of multi-beam [16], [20], [22], [31]–[33] or of transverse oscillation [24], [25] approaches, the accuracy is known to be worse at great depths due to the limited physical aperture of the arrays [34]. However, PW-based speckle-tracking methods, exploiting either 2D cross correlation [23], [35] or different velocity estimators [7], [36], [37], are not expected to be affected by such problems.

The goal of this chapter was to assess to what extent the performance of a vector Doppler method depends on the investigation depth, and whether such dependence is related to the specific method under consideration or is due to more general aspects such as the characteristics of the transmitted beam. To reach this goal, two methods have been considered: the 2D-VFI method illustrated in paragraph 2.3 , as representative of the new class of approaches based on PW Tx, and the multigate spectral Doppler method, see paragraph 2.2 , based on focused Tx, which has so far represented the gold-standard for axial velocity measurements.

For both these reference methods, simulations were done to evaluate the velocity estimation accuracy obtainable at different depths, Doppler angles and transmission schemes (focused beams and plane waves). Simulated transmitted beams were also compared to those experimentally measured and correlated with the estimation performance.

Simulation and experimental results provide evidence that the transmitted beam shape, rather than the measurement method, plays a fundamental role on the mentioned velocity underestimation. An alternative design of the acoustic lens is thus proposed to tailor the ultrasound beam when investigating blood flow over a wide range of depths of interest.

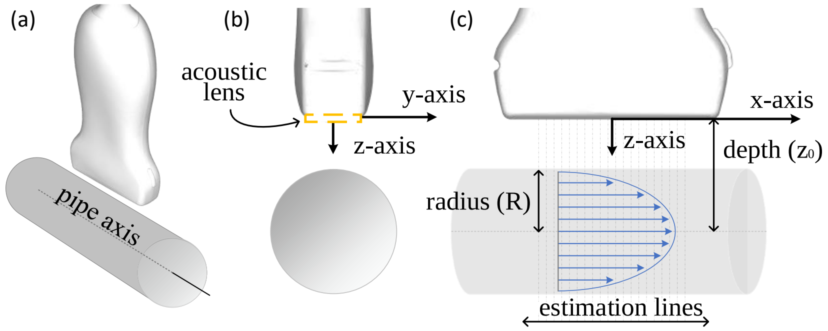

Fig. 4-1 Reference system for simulations by three point of views: isometric (a), Y-Z plane (b) and X-Z plane (c).

4.2 Methods

4.2.1 Simulation Setup

Simulations were conducted by Simag and Field II. As summarized in Table 4.I, the simulated linear array consisted of 192 elements, whose size was 0.215×6 mm and with pitch of 0.245 mm. Fig. 4-1 shows the reference system setup. Two versions of the same linear array were simulated:

1) with an acoustic lens focused at 18 mm;

2) with an unfocused (flat) lens.

In transmission, 5-cycle sinusoidal bursts, centered at $f_0 = 6\ MHz$ and tapered by a Hamming window, were used. Two focusing schemes were considered:

1) Plane waves (PW) - 128 active elements were simultaneously excited;

2) Focused beams (FBs) - the f-number was set to ≈ 4, by modulating the number of transmission elements according to the different focal depths (20, 40, 60, 80, and 100 mm).

The transmitted ultrasound fields over the lateral (xz) and elevation (yz) planes were simulated. Then, simulations were conducted for 500 consecutive transmission events, with a pulse repetition frequency of 2500 Hz (equivalent to 0.2 s), on both parabolic and flat steady flows, with peak velocity of 15 cm/s. The numeric phantom simulated a 4-mm radius (R), wall-less, cylindrical tube, whose density was 25 scatterers per mm^3, which was placed at a distance z_0 , see Fig. 4-1 (c), of 20, 40, 60, 80, and 100 mm far from the probe with three different Doppler angles (ϑ_D= 90°, 82.5° and 75°).

In reception, the simulated echo data were sampled at 50 MHz, corresponding to an axial step between consecutive samples (δ_z) of 15.4 μm. The number of receiving elements was set to 128 for all cases, with a dynamic apodization at constant f-number equal to 2. When transmitting PWs, for each transmission event, 64 lines centered on the probe axis were beamformed with a lateral pitch equal to $\delta_x = 0.245$ mm, i.e. coincident with the array pitch. When transmitting FBs, only the line corresponding to the probe axis was beamformed.

TABLE 4.I

MAIN SETTINGS IN SIMULATION

Probe Parameters	
Transducer	Linear Array
Number of Elements	192
Pitch [mm]	0.245
Central Frequency [MHz]	8
6dB Bandwidth	114%
Elevation Focus [mm]	18 (Focused lens), Inf (Flat lens)
System Parameters	
Speed of Sound (c) [m/s]	1540
Tx Central Frequency (f_0) [MHz]	6
Rx Sampling Frequency (f_c) [MHz]	50
Axial distance between consecutive RF samples (δ_z) [μm]	15.4
Pulse Repetition Frequency (PRF) [Hz]	2500
Blood Flow Parameters	
Inner Radius (R) [cm]	4
Beam-to-Flow Angle (ϑ_D) [°]	90, 82.5, 75
Flow axis depth (z_0) [mm]	20, 40, 60, 80, 100
Peak Velocity (v_p) [cm/s]	15
Scatterers Density [1/mm^3]	25

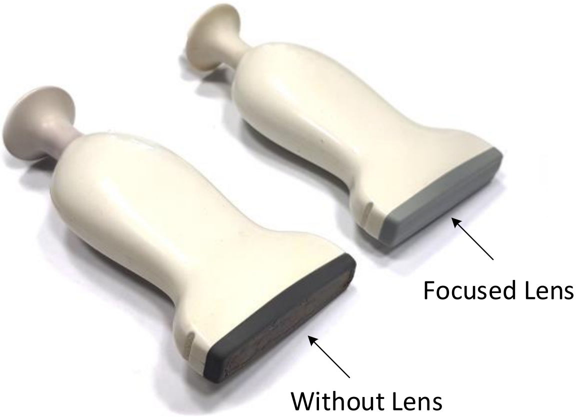

Fig. 4-2 The two linear-array probes used for the experiments. For one of them (left), the focused lens was removed and replaced with a matching layer.

4.2.2 Experimental Setup

In order to experimentally verify simulations, two linear array probes (model LA533, Esaote, Florence, Italy), having the same characteristics of the simulated arrays, were used. The first one was the commercial version of the probe, while on the second one the acoustic lens was removed and equipped with a flat matching layer, as shown in Fig. 4-2.

The main system parameters are summarized in Table 4.I. The ULA-OP 256 was programmed to transmit 5 cycles of sinusoidal busts at 6 MHz by 128 elements, with a PRF of 1 kHz. In reception, signals were sampled at 39 MHz and 64 lines, centered on the probe aperture, were beamformed as for simulation tests, see paragraph 4.2.1 .

One-way fields measurements (in X-Z and Y-Z surfaces) were conducted in a water tank, moving the probe under test, with a custom controlled positioning system (configurable with Matlab script), and recording the transmission pressure field with a hydrophone HGL-0400 (Onda, Sunnyvale, CA USA). Maximum absolute pressure values were acquired on a 1-mm step grid of 51 × 101 samples, giving an overall scanning area of 50 × 100 mm2.

A homemade phantom was used, in which a blood-mimicking fluid flew in a cylindrical Rilsan® pipe immersed in a water tank, as shown in Fig. 4-3. The fluid was obtained by stirring 3 g of 10 μm polyamide

TABLE 4.II

MAIN EXPERIMENTAL SETTINGS

System Parameters	
Tx Central Frequency (f_0) [MHz]	6
Rx Sampling Frequency (f_c) [MHz]	39
Axial distance between consecutive RF samples (δ_z) [µm]	19
Pulse Repetition Frequency (PRF) [Hz]	1000
Number of Tx/Rx Elements	128
Beamformed Lines	64
Blood Flow Parameters	
Inner Radius (R) [cm]	4
Beam-to-Flow Angle (ϑ_D) [°]	90
Flow axis depth (z_0) [mm]	20, 40, 60, 80, 100
Peak Velocity (v_p) [cm/s]	8

spherical particles (Orgasol®, Arkema Inc., Philadelphia, PA) in 2 L of demineralized water until a homogeneous suspension was achieved (density of 2.6 × 1010 scatterers/mm3). The flow was forced by a peristaltic pump connected to a pulsation dampener, capable of further reducing possible turbulences. Considering the entrance length of the tube

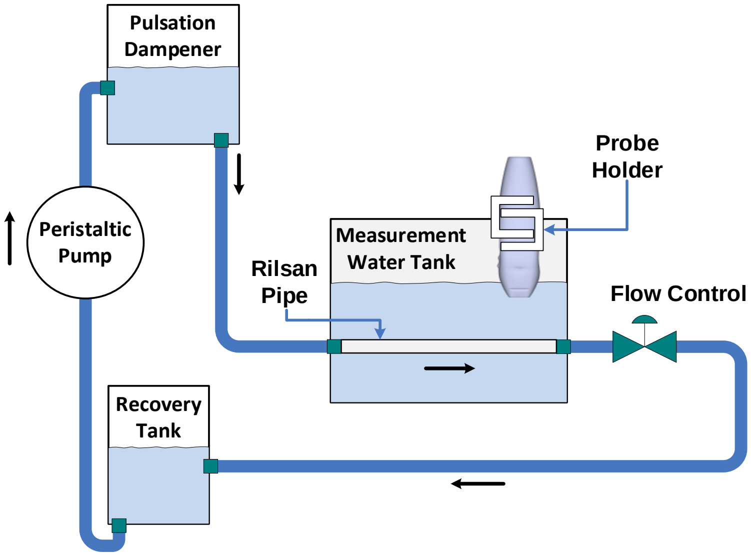

Fig. 4-3 Schematic diagram of the flow phantom. Black arrows define the flow direction inside the pipes, represented as blue lines.

(70 mm), parabolic flow was guaranteed by setting the peak velocity approximately at 8 cm/s. Acquisitions were conducted considering the same depths of interest used in simulation [20, 40, 60, 80, 100] mm with a Doppler angle of ϑ_D=90°.

4.2.3 Processing Setup

2-D Vector Flow Imaging

In PW imaging mode, the flow velocities were estimated through 2-D HFR VFI based on RF data (see paragraph 2.3). The size of the estimation kernel was set to (z, x) 196 × 22 samples. Each kernel was weighted with a Hann's window in both directions, reaching the effective size of 1.5 × 2.5 mm. Adjacent kernels were overlapped of 92% and 95% along the z direction and x-axis, respectively. According to these settings, 43 velocity profiles over the region of interest (ROI) were reconstructed. The DFTs were calculated with n_{f_z}=3 and n_{f_x}=10 different frequencies, along z-axis and x-axis, respectively.

Multigate Spectral Doppler Processing

Signals beamformed along the central line of the probe, for both PWs and FBs, were processed according to multigate spectral Doppler

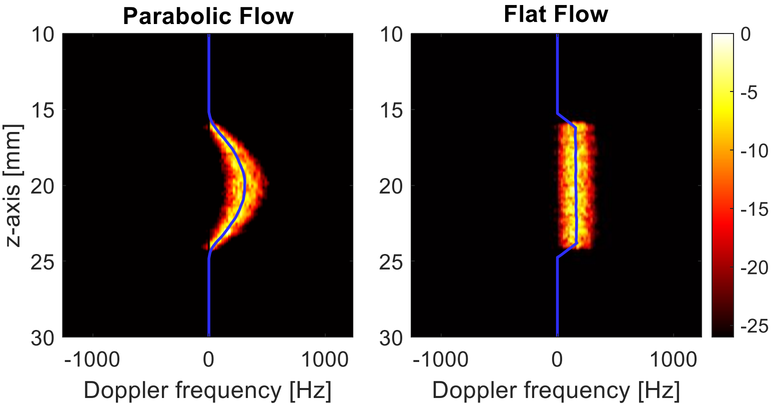

Fig. 4-4 Example of the MSD obtained in simulation for parabolic (on left and flat (on the right) flows, located at 20 mm of depth. The colormap represent the spectra amplitude (dB) normalized for the maximum value.

processing. For each gate, the analytic (i.e. Hilbert transformed) signals were gated, in the slow time direction, with blocks of 128 points. The overlapping between two consecutive point selections was set to 88%. The frequency domain conversion was made by a 128-point fast Fourier transform (FFT). Hence, from the 500 transmission events, 17 multigate spectral Doppler frames were obtained and finally averaged. Those spectra were further processed to extract the weighted mean frequency, which was used to compute the estimated flow velocity, according to the Doppler equation and given the Doppler angle. An example of the MSD is shown in Fig. 4-4.

4.2.4 Performance Metrics

The estimation accuracy and precision were assessed in terms of mean relative bias and standard deviation of velocity estimates, as proposed in [29]. The relative bias expresses the average relative error of the measurement with respect to the reference, while the standard deviation quantify how stable is the measurement over time. For each point of

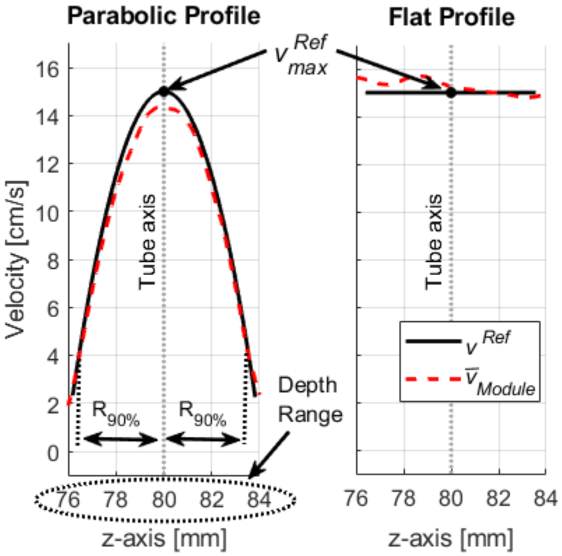

Fig. 4-5 Example of parabolic (left) and flat velocity profiles (right) estimated by simulations (red dash lines). The reference profiles are represented as solid black lines.

interest $P(z_p, x_p)$, located at a distance shorter than 90% of the pipe radius from the flow axis ($R_{90\%}$ in Fig. 4-5), the mean relative bias of each estimated velocity module (v_{Module}) was defined as:

$$\bar{B}_v = \frac{1}{v_{max}^{Ref}} \frac{1}{N_p} \sum_{p=1}^{N_p} \left(v^{Ref}(z_p, x_p) - \bar{v}_{Module}(z_p, x_p) \right) \qquad (4.1)$$

where v^{Ref} is the reference profile (parabolic or flat) with v_{max}^{Ref} = 15 cm/s of peak velocity and N_p is the number of selected points.

The mean relative standard deviation was calculated as

$$\bar{\sigma}_v = \frac{1}{v_{max}^{Ref}} \sqrt{\frac{1}{N_p} \sum_{p=1}^{N_p} \sigma_{vModule}(x_p, z_p)^2} \qquad (4.2)$$

where

$$\sigma_v(x_p, z_p) = \sqrt{\frac{\sum_{u=1}^{N_F} \left(v_{Module}(x_p, z_p, t_u) - \bar{v}_{Module}(x_p, z_p) \right)^2}{(N_F - 1)}} \qquad (4.3)$$

is the standard deviation evaluated for each velocity component averaged over the total number of frames N_F.

4.3 Results

4.3.1 Simulated One-way Fields with Focused Lens

Fig. 4-6 shows the one-way fields on the lateral plane (x-z), simulated for six transmission settings: 5 FBs with focal distance at 20, 40, 60, 80 and 100 mm, and the PW beam. As expected, the (-6dB) beamwidth at the focal depth of FBs is constant (1.25±0.1 mm), as the f-number was kept

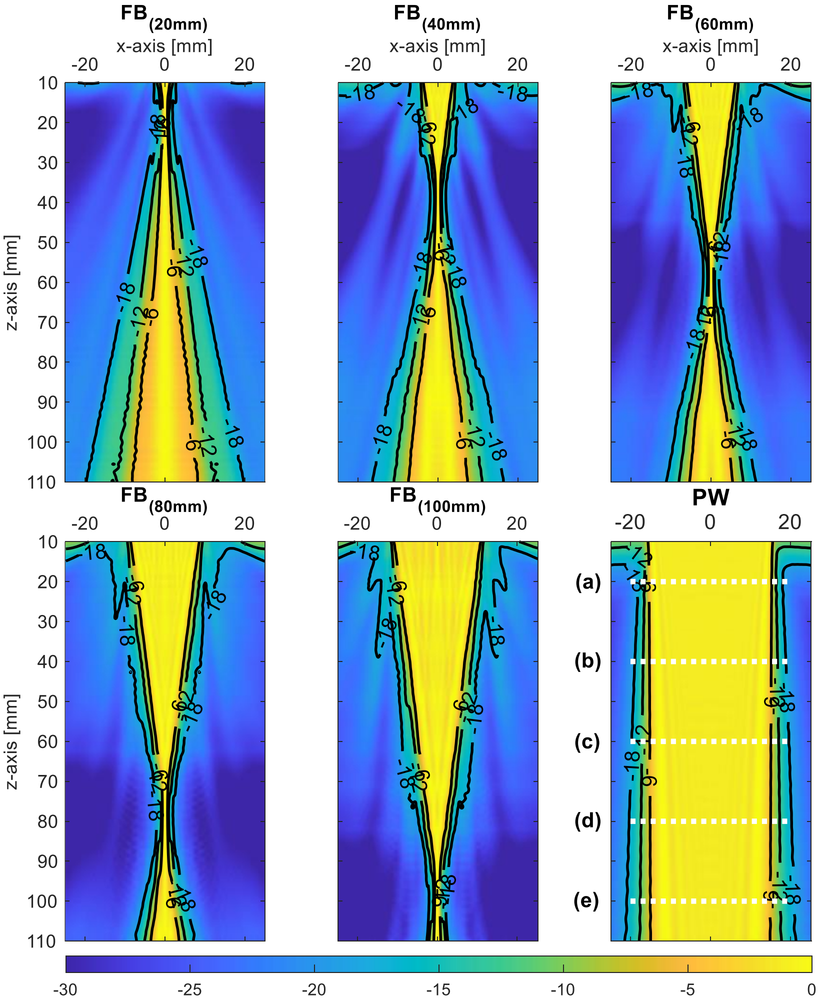

Fig. 4-6 One-way fields simulated on x-z plane for FB with focal distances at 20,40,60,80, 100 mm and PW. Fields were normalized by their maximum at each depth and their magnitude was color coded in dB.

the same. For the PW, the transmitted beam keeps well its width on the lateral direction for all analyzed depths.

Fig. 4-7 shows the one-way fields simulated on the elevation plane (y-z) for the six transmission settings used with the array equipped with focused lens. Although, the beams were focused at different depths on the x-z plane, this did not impact on the beam profile along the y-z plane,

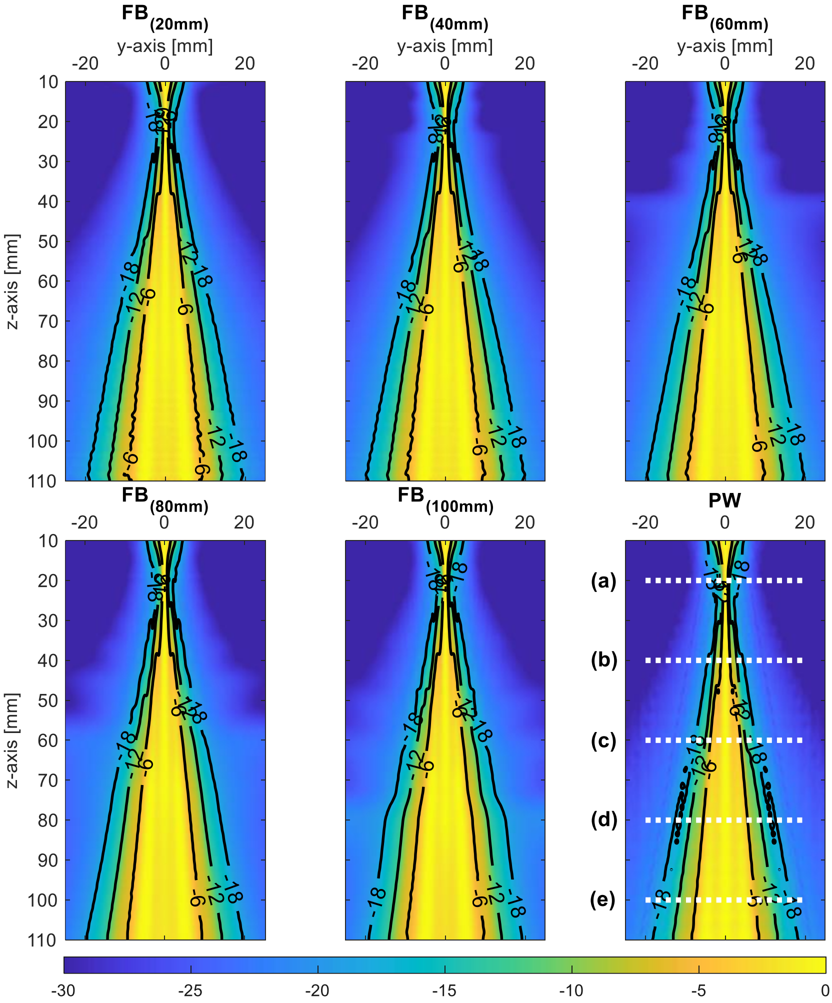

Fig. 4-7 One-way fields simulated on y-z plane for Focused Beams with focal distances at 20,40,60,80, 100 mm and PW. Fields were normalized by their maximum at each depth and their magnitude was color coded in dB.

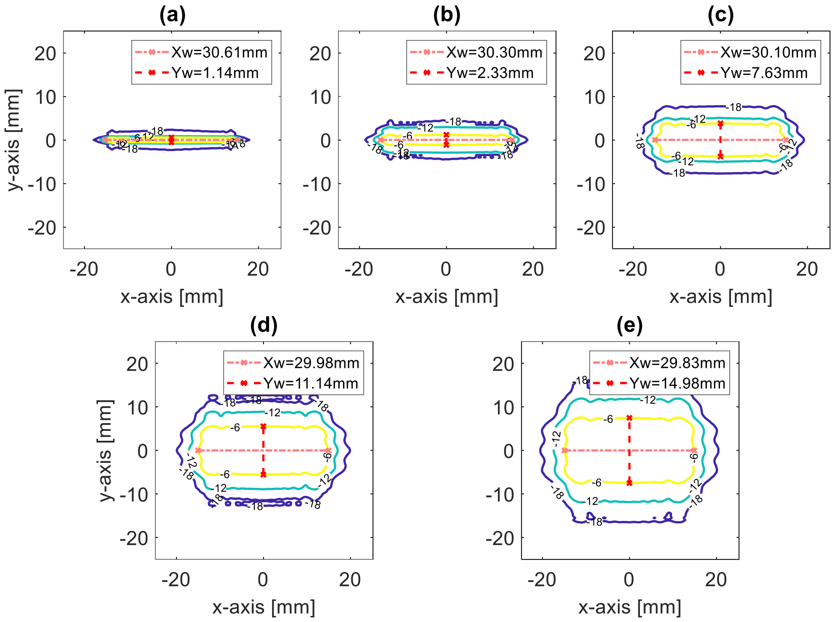

Fig. 4-8 Isolines of beamplots on planes parallel to the probe surface at 5 depths: (a) 20mm, (b) 40mm, (c) 60mm, (d) 80mm, (e) 100mm.

which is forced only by the acoustic lens, and, beyond the focal length of the lens (18 mm), highlights a progressive broadening due to diffraction.

Quantitatively, the beam spread was evaluated at 5 reference depths: (a) 20mm, (b) 40mm, (c) 60mm, (d) 80mm, (e) 100mm, highlighted in Fig. 4-6 and Fig. 4-7.

The 5 panels of Fig. 4-8 (a)-(e) report the isolines (at -6dB steps) of the beamplots estimated on planes parallel to the probe surface (x-y), for the PW transmission. On the lateral direction, the width is Xw=30.61 mm at 20 mm and reduces by only 2.5 % at 100 mm, where it reaches Xw=29.83 mm. On the other hand, on the y-direction, the beam width, starting from Yw=1.14 mm at 20 mm, reaches Yw=14.98 mm at 100 mm, i.e. a widening of 1300%. It is worth highlighting that the -6dB width at 6 cm of depth (Yw = 7.63 mm) is already comparable to the diameter of the simulated vessel (8 mm). On the y-direction, similar results were obtained also for the focused beams.

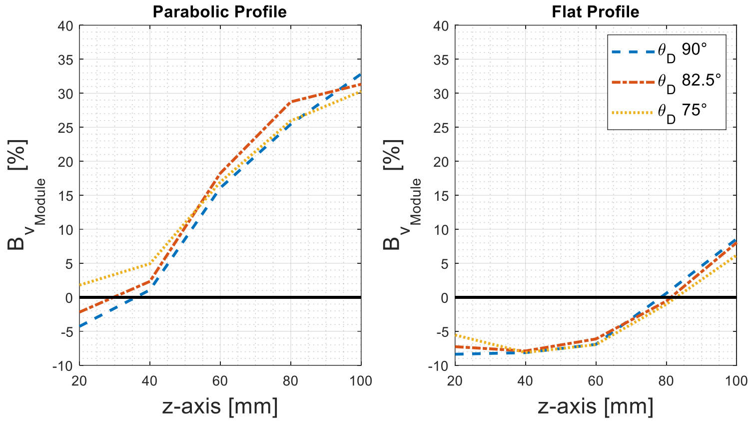

Fig. 4-9 Estimation bias at different depths for both parabolic (left) and flat (right) flows, with three different Doppler angles.

4.3.2 Performance of 2D-VFI at Different Depths

Fig. 4-9 shows the mean relative bias estimated at 5 depths with 3 Doppler angles, for both velocity profiles (parabolic and flat). The relative errors and standard deviations of the velocity modules are also listed in Table 4.III. Parabolic flow results show that 2-D VFI is reasonably accurate (-4.3% < $\bar{\boldsymbol{B}}_{v_{Module}}$ < 4.9%) for depths up to 4 cm. However, a considerable (16.1% < $\bar{\boldsymbol{B}}_{v_{Module}}$ < 32.8%) depth dependent underestimation is noted at higher depths. On the other hand, for a flat profile, 2-D VFI is always reasonably accurate at all depths and Doppler angles (-8.4% < $\bar{\boldsymbol{B}}_{v_{Module}}$ < 8.6%).

TABLE 4.III

LA533 WITH FOCUSED LENS:

RELATIVE BIAS AND MEAN STANDARD DEVIATION FOR 2-D VFI SIMULATIONS.

Depth [mm]	**Parabolic Flow** $\bar{\boldsymbol{B}}_{v_{Module}} \pm \bar{\boldsymbol{\sigma}}_{v_{Module}}$ [%]			**Flat Flow** $\bar{\boldsymbol{B}}_{v_{Module}} \pm \bar{\boldsymbol{\sigma}}_{v_{Module}}$ [%]		
	ϑ_D=90°	**ϑ_D=82.5°**	**ϑ_D=75°**	**ϑ_D=90°**	**ϑ_D=82.5°**	**ϑ_D=75°**
20	-4.3±2.1	-2.2±3.3	1.8±5	-8.4±2.2	-7.3±3	-5.5±6.2
40	1.1±2.4	2.3±3.5	4.9±5.6	-8.1±2.1	-7.9±2.4	-8.1±5.4
60	16.1±3.4	18.2±5.4	17±7.8	-6.9±2.2	-6.1±2.2	-7±7.6
80	25.4±3.5	28.7±6	25.9±9.7	0.6±2.3	-0.6±2.5	-1±4.2
100	32.8±3.7	31.3±6	30.3±9.6	8.6±2.3	8.1±2.7	6.2±3.3

4.3.3 Performance of Multigate Spectral Doppler at Different Depths

The accuracies assessed for the MSD with both FBs and PW transmissions (reported in Table 4.IV and Table 4.V, respectively) showed similar results. Specifically, for the parabolic profile, $\overline{\boldsymbol{B}}_{v_{Module}}$ is higher than 10% for depths greater than 60 mm, and reaches roughly 25% at 100 mm with a Doppler angle of 75°. On the other hand, for the flat flow, $\overline{\boldsymbol{B}}_{v_{Module}}$ is always included in the interval ±5%, and there is no noticeable dependence with depth. These trends are comparable with those shown in Table 4.III for 2-D VFI, which however has slightly higher $\overline{\boldsymbol{B}}_{v_{Module}}$.

TABLE 4.IV

RELATIVE BIAS OF MSD WITH FOCUSED TRANSMISSIONS

Depth [mm]	**Parabolic Flow** $\overline{\boldsymbol{B}}_{v_{Module}}$[%]		**Flat Flow** $\overline{\boldsymbol{B}}_{v_{Module}}$ [%]	
	ϑ_D=82.5°	**ϑ_D=75°**	**ϑ_D=82.5°**	**ϑ_D=75°**
20	-3.02	-1.28	-4.57	-1.31
40	1.68	5.59	-3.61	-1.67
60	13.10	18.76	-3.06	-1.59
80	17.18	23.47	-3.39	-1.78
100	22.82	25.61	-0.91	-0.92

TABLE 4.V

RELATIVE BIAS OF MSD WITH PW TRANSMISSIONS

Depth [mm]	**Parabolic Flow** $\overline{\boldsymbol{B}}_{v_{Module}}$[%]		**Flat Flow** $\overline{\boldsymbol{B}}_{v_{Module}}$ [%]	
	ϑ_D=82.5°	**ϑ_D=75°**	**ϑ_D=82.5°**	**ϑ_D=75°**
20	-2.87	0.35	-3.93	-0.14
40	0.65	5.55	-2.75	0.66
60	10.76	16.75	-2.10	-1.35
80	16.96	22.37	-1.43	-0.50
100	19.56	25.27	0.92	0.37

4.3.4 Effect of the Acoustic Lens

On one-way fields

The one-way fields produced by the array with unfocused lens on lateral and elevation planes are shown in Fig. 4-10. While the beam on the x-z plane does not differ from that shown in PW panel of Fig. 4-6 for the focused lens, the beam on the y-z plane is significantly more uniform and does not broaden progressively. As shown in Fig. 4-11 in the y-direction the beam width Yw is in the range [3.73, 5.38] mm, with its maximum at 20 mm. On the x-z plane, the width Xw is quite stable with the depth: 30±0.5 mm.

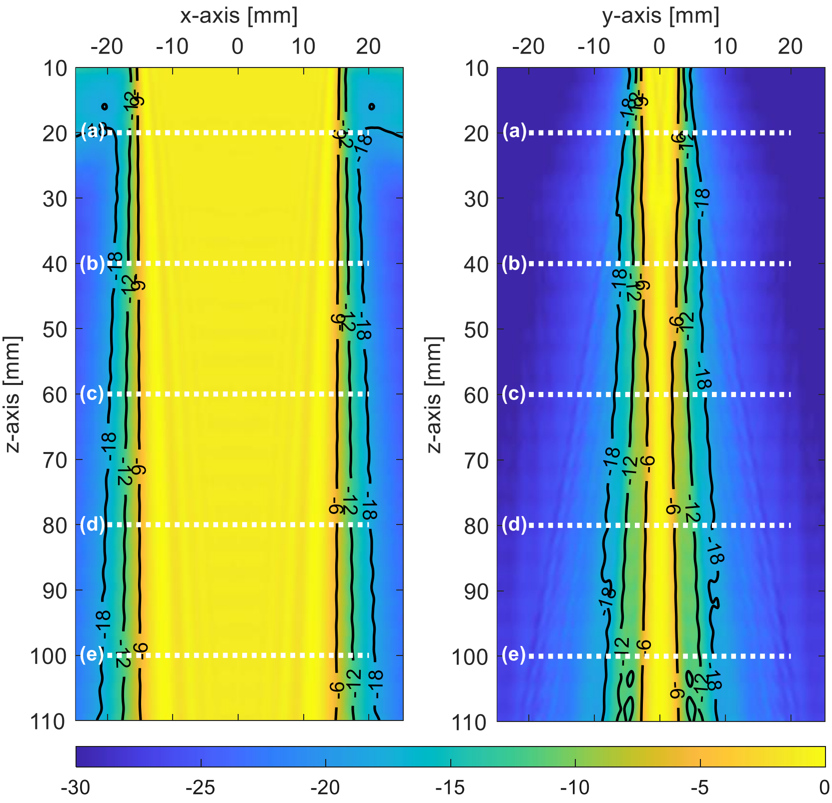

Fig. 4-10 One-way fields simulated for x-z (on left side) and y-z (on right) planes for the linear array probe with unfocused lens. Fields were normalized by their maximum at each depth and their magnitude was color coded in dB.

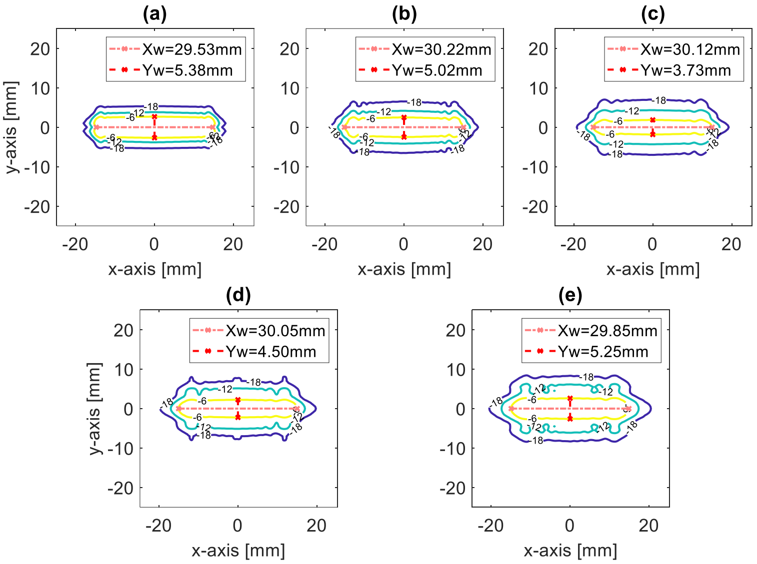

Fig. 4-11 Isolines of beamplots on planes parallel to the unfocused lens probe surface at 5 depths: (a) 20mm, (b) 40mm, (c) 60mm, (d) 80mm, (e) 100mm.

On 2D-VFI performance

Fig. 4-12 shows the estimated mean relative bias evaluated at 5 depths with 3 Doppler angles, for both velocity profiles (parabolic and flat). The relative errors and standard deviations of the velocity modules are also listed in Table 4.VI. Parabolic flow results show that 2-D VFI is always reasonably accurate (1.7% < $\overline{\boldsymbol{B}}_{\boldsymbol{v}_{\boldsymbol{Module}}}$ < 14.9%) with the best performance at 60 mm and the worst at 100 mm. Also for a flat profile, 2-D VFI is always reasonably accurate at each depth and Doppler angle (-9% < $\overline{\boldsymbol{B}}_{\boldsymbol{v}_{\boldsymbol{Module}}}$ < 9.2%).

Fig. 4-13 qualitatively compares the velocity profiles obtained with the focused and the unfocused lens. The figure shows that for the focused lens (blue line), a high underestimation is already noted at 60 mm, and is even more marked at 100 mm. On the other hand, the unfocused lens (red line) allows better estimates at higher depths, although not at 20 mm, and the underestimation is less depth dependent.

Table 4.VI

LA533 with Unfocused Lens:

Relative Bias and Mean Standard Deviation for 2-D VFI Simulations.

Depth [mm]	**Parabolic Flow** $\bar{B}_{v_{Module}} \pm \bar{\sigma}_{v_{Module}}$ [%]			**Flat Flow** $\bar{B}_{v_{Module}} \pm \bar{\sigma}_{v_{Module}}$ [%]		
	ϑ_D=90°	**ϑ_D=82.5°**	**ϑ_D=75°**	**ϑ_D=90°**	**ϑ_D=82.5°**	**ϑ_D=75°**
20	6.5±2.6	8.1±3.4	12±5.2	-9±2.3	-7.9±2.7	-5.6±6.7
40	3.4±2.5	3.9±3.5	6.6±5.6	-8.8±2.3	-8±2.5	-7.5±5.4
60	1.7±2.2	4.7±3.7	4.3±5.8	-7±1.8	-6.6±1.9	-5.9±5.3
80	5.8±2.1	7.5±3.4	8.5±6	-1±2.2	-0.5±2.1	-0.4±3.7
100	13.6±2.4	14.9±4.2	12.9±5.8	9.2±2.3	8±2.8	6.7±4.5

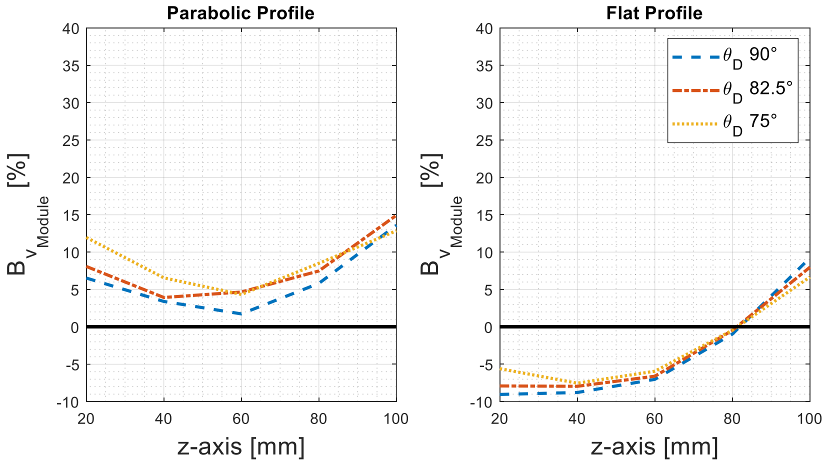

Fig. 4-12 Estimation bias obtained with unfocused lens, at different depths for both parabolic (left)and flat (right) flows, with three different Doppler angles.

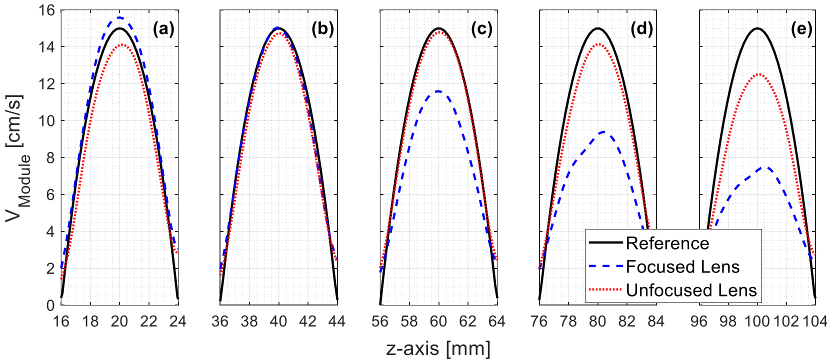

Fig. 4-13 Modules of the parabolic profiles ($\vartheta_D = 90°$) estimated at 5 depths ((a) 20mm, (b) 40mm, (c) 60mm, (d) 80mm and (e) 100mm), using both the focused lens (blue dashed line) and the flat one (red dotted line). The reference simulated profile is reported in black.

4.3.5 Experiments

One way-fields

The experimental one-way fields are shown in Fig. 4-14. Qualitatively, the beams on the y-z plane respect the trends observed in simulation in Fig. 4-7 and Fig. 4-10. The probe with a focused lens shows a prominent broadening of the beam in the y-direction after the focal distance while the probe without lens seems to be more homogeneous. On the x-z plane the behaviors are similar for the two probes, with a slight narrowing of the beam with increasing depths. These results are quantitatively confirmed by the isolines on planes parallel to the probe surface (x-y) reported in Fig. 4-15. With the focused lens, the beamwidth on y-direction goes from its minimum, Yw=1.1 mm, at 20mm to its maximum, Yw=17.29, at 100mm of depth. Without the lens, Yw remains between 3.37 mm, at 40 / 60 mm, and 5.48 mm, at 100 mm. On the x-direction, with or without acoustic lens, the beam slightly narrows from Xw = 29 mm (28 mm without lens) to about 25.5 mm.

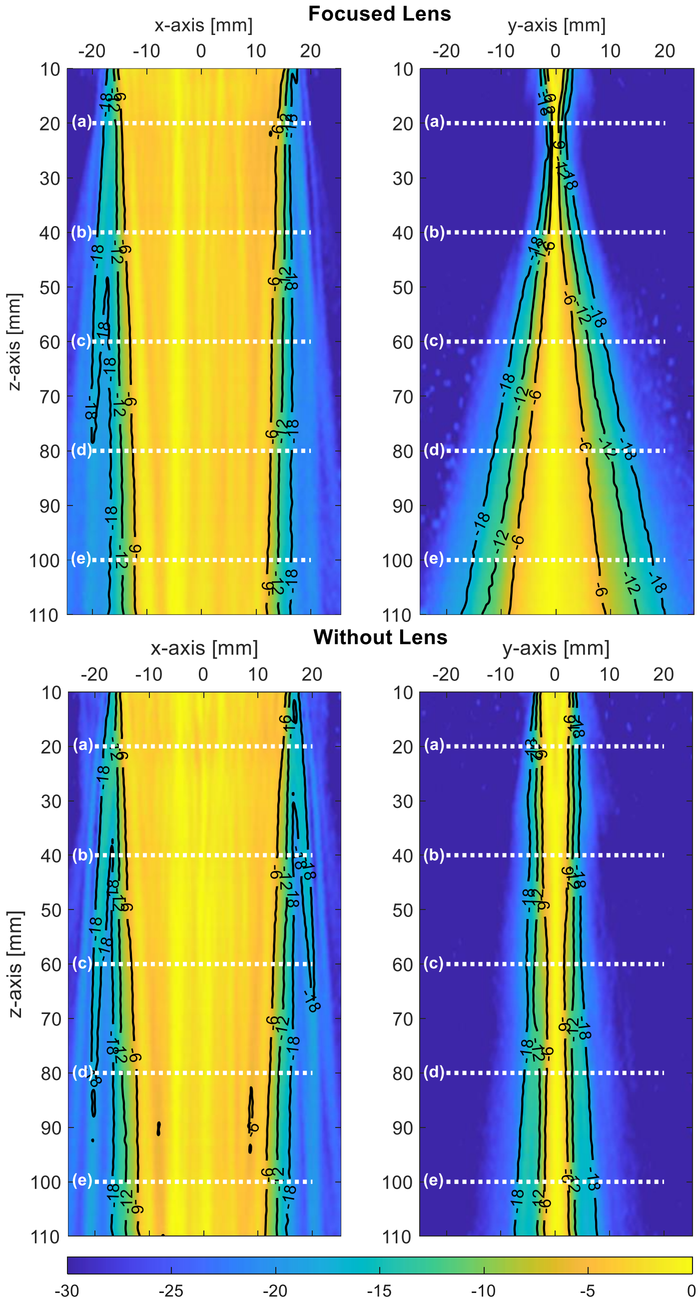

Fig. 4-14 One-way fields acquired for x-z (on left column) and y-z (on right) planes for the linear array probes with focused (on top) and without (bottom) lens. Fields were normalized by their maximum at each depth and their magnitude was color coded in dB.

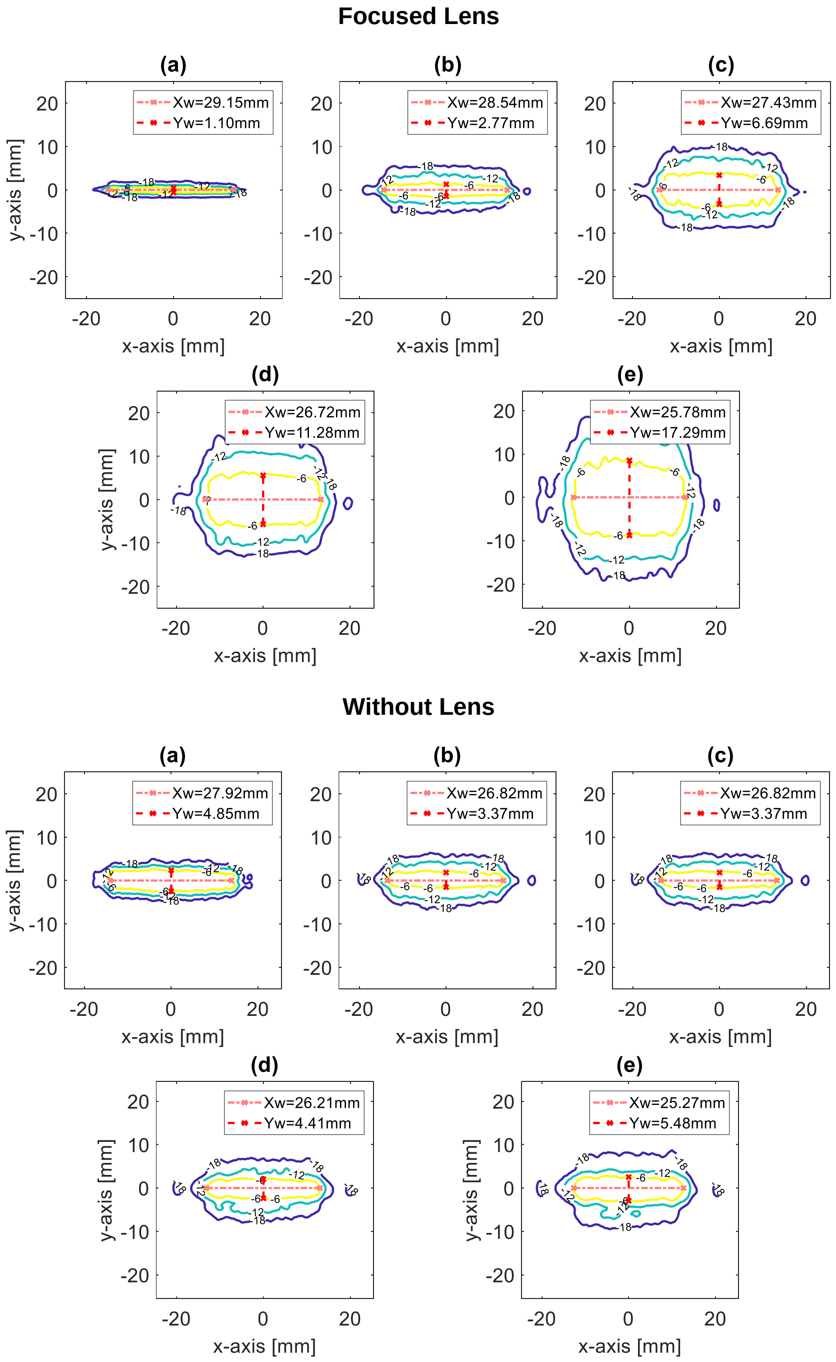

Fig. 4-15 Isolines of beamplots on planes parallel to the probe surface at 5 depths: (a) 20mm, (b) 40mm, (c) 60mm, (d) 80mm, (e) 100mm. Isolines were obtained with both the probes: with (top) and without (bottom) focused lens.

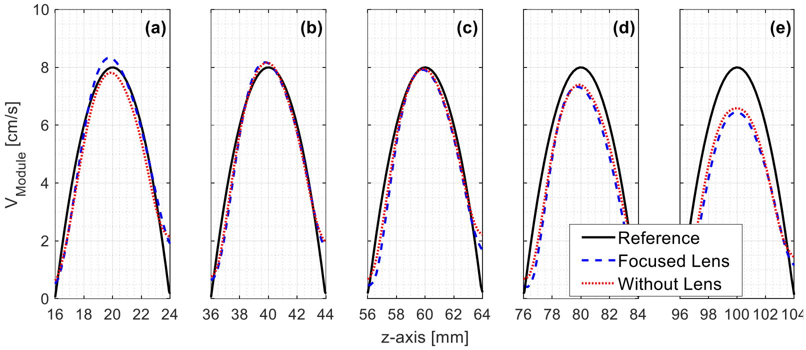

Fig. 4-16 Modules of the parabolic profiles (ϑ_D = 90°) estimated on experiments at 5 depths ((a) 20mm, (b) 40mm, (c) 60mm, (d) 80mm and (e) 100mm), using both probes: with (blue dashed line) and without (red dotted line) focused lens. The reference profile is shown in black.

2D-VFI performance

Fig. 4-16 allows comparing the velocity profiles obtained for probes with (blue line) and without (red line) the focused lens. The estimated velocity profiles are very similar at all depths. In particular, the estimation looks very accurate up to 60 mm, while it worsens at 80 and 100 mm.

Quantitatively, Fig. 4-17 and Table 4.VII show the mean relative bias evaluated at 5 depths, for both probes. As expected, the probe with the focused lens performs better at 20 mm ($\bar{B}_{v_{Module}}$= -1.2% vs 5.1%). At

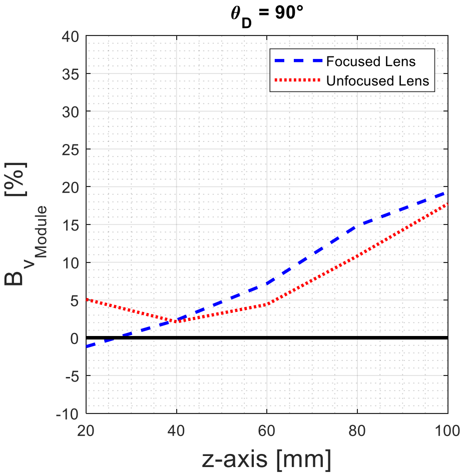

Fig. 4-17 Estimation bias obtained with and without lens at different depths with 90° Doppler angle.

TABLE 4.VII

RELATIVE BIAS AND MEAN STANDARD DEVIATION FOR EXPERIMENTS.

Depth [mm]	**Focused Lens** $\bar{B}_{v_{Module}} \pm \bar{\sigma}_{v_{Module}}$ [%]	**Without Lens** $\bar{B}_{v_{Module}} \pm \bar{\sigma}_{v_{Module}}$ [%]
	ϑ_D=90°	**ϑ_D=90°**
20	-1.2 ±3.1	5.1 ±3.1
40	2.3 ±3.4	2.1 ±3.3
60	7.2 ±4	4.4 ±3.6
80	14.8 ±4.4	10.8 ±4.3
100	19.3 ±5	17.7 ±4.7

40 mm, the two probes perform similarly ($\bar{B}_{v_{Module}}$= 2.3% vs 2.1%), while for higher depths the probe without lens performs better ($\bar{B}_{v_{Module}}$=19.3% vs 17.7% at 100 mm).

4.4 Discussion and Conclusion

This chapter has presented a detailed study on the accuracy attainable with 2D-VFI methods based on the transmission of plane waves, when estimating blood flow at great investigation depths. The study was based on both simulation and experimental tests, considering linear array probes equipped with different acoustic lenses.

Simulation results (Fig. 4-9 and Table 4.III) show that 2-D VFI strongly underestimates flow speeds at investigation depths greater than 40 mm, reaching a bias up to 30% at 100 mm. Such underestimation is marked only for the parabolic flow profile, whereas, for the flat flow profile, the underestimation is more restrained and less depth dependent. Hence, in order to assess to what extent such underestimation at great depths should be ascribed to the specific 2D VFI method, simulations and experiments were performed and the results compared to those obtained with multigate spectral Doppler, i.e. the gold standard Doppler method. Simulations show that even though MSD based on either FBs and PWs perform slightly better than 2-D VFI, the underestimation at great investigation depths is still significant (see Table 4.IV and Table 4.V). As for 2D-VFI, the underestimation is marked only for the parabolic profile (up to a bias of 25%), but it is limited for the flat profile. These results highlight that there is, actually, a contribution to the underestimation by the method, which makes 2D-VFI performing worse than MSD, but a major contribution should be ascribed to other sources.

Concerning the method contribution, it should be considered that for 2D-VFI, the velocity module is obtained by the estimation of two velocity components, axial and lateral, which are affected by different estimation biases. Specifically, it is known that 2D-VFI methods, being limited by the lateral resolution and the kernel size, produce worse estimates of the lateral velocity components. On the other hand, MSD only estimates the axial velocity component, while the module is obtained trigonometrically when the Doppler angle is known. Since, in simulation, the Doppler angle is known, the velocity module obtained with MSD result accurate. However, in in-vivo applications, this angle is provided either manually by the operator, or by means of advanced tracking systems. The error deriving from the wrong estimation of the Doppler angle dramatically affects the flow velocity estimate, as widely discussed in the literature [38]. For example, with $\vartheta_D = 80°$, an error of 1° on the Doppler angle, results in a 10% error on the velocity estimate.

To find possible other sources of contribution to the underestimation, one-way field simulations were conducted. These highlighted that, regardless the focal distance, the beam on the elevation plane show a progressive broadening, forced by the acoustic lens. In fact, such a beam broadening yields huge “sample volumes” contributing to the received echo signal. Hence, all velocities of particles in the sample volume are averaged the flow velocity is estimated. Since a parabolic flow involves a spatial velocity gradient, the average flow speed is decreased by the presence of components at lower velocity in the sample volume. This hypothesis is also confirmed by the tests carried out for the flat flow, which is characterized by a constant velocity distribution over the entire vessel. In this case there is no spatial velocity gradient and the underestimation is considerably reduced at great depths.

Given the above observations, it was supposed that an acoustic lens producing a less depth-dependent beamwidth could improve the estimation of flow velocity at great depths. Hence, an alternative design of the acoustic lens has been tested. A second linear array was simulated; it was equipped with a flat lens, i.e. a not focused lens. It turned out to be effective in limiting the beam broadening on the elevation plane, as shown in Fig. 4-10 and Fig. 4-11. Moreover, the depth dependency, for the parabolic profile, was less marked (see Fig. 4-12 and Table 4.VI), than that obtained with the focused lens, being always lower than 15%. Besides, for the flat profile, the trend of the biases, obtained with both focused and flat lenses, were very similar.

Experimental tests were also conducted. The commercial LA533 probe (with focused lens) and its customized version (without lens) were tested for PW transmission and for 2D-VFI. As in simulation, acquired one-way fields (Fig. 4-14) confirmed that with the focused lens the acoustic beam on the elevation plane progressively broadens, while, without the focused lens, the beam broadening is considerably limited.

Experimental VFI tests confirmed that, comparing the probe with or without the focused lens, the former perform better at the focal distance of the lens, but worse at depths higher than 60 mm (Fig. 4-17 and Table 4.VII). However, differently from simulations, it seems that the effect of the beam broadening on the underestimation is less detrimental. Indeed, for example, while in simulation at 100 mm the difference between the $\bar{B}_{v_{Module}}$ obtained with and without lens was in average $32.8\% - 13.6\% = 20.8\%$, in acquisitions the same difference is $19.3\% - 17.7\% = 1.6\%$. Hence, it seems that the actual probe with focused lens perform better than what expected from simulations. However, such deviation should be ascribed to a limitation of the experimental flow phantom. Indeed, at the interface between water and Rilsan® most of the energy is not transmitted inside the tube but reflected or refracted [39], [40]. This effect has a major impact on the beam generated by the focused lens, which reaches the Rilsan tube with several incidence angles. In practice, the tube transmits inside the tube only the incident energy with smaller incidence angles, as a kind of re-focusing or re-tailoring of the broad beam. This effect implies a smaller sample volume and the lowest flow velocities, closer to the walls, do not compromise the velocity estimation. Currently, a pipe in PVA is under development and additional experimental tests will be conducted to confirm simulation findings.

In conclusion, this chapter has shown that there is a strict correlation between the shape of the beam produced by the array on the elevation plane and the results of velocity estimations. If such estimations must be extended over a large range of depths, the acoustic lens should be correspondingly designed with focusing limited as much as possible. It is worth highlighting that all the above considerations also impact on 3D-VFI, which is typically based on the transmission of plane or, even worse, diverging waves [41]–[44]. Nevertheless, the problem could here be partially alleviated considering that 2D probes allow dynamic beamforming in reception on both lateral and elevation directions.

Chapter 5. 3-D Vector Flow Imaging in the Frequency Domain

Ultrasound vector Doppler techniques for three-dimensional (3-D) blood velocity measurements are currently limited by low temporal resolution and high computational cost. This chapter presents an efficient 3-D high-frame-rate vector Doppler method, which estimates the displacements in the frequency domain.

The activity reported in this chapter resulted in the following publications:

***S. Rossi**, A. Ramalli, F. Fool and P. Tortoli, "**High-Frame-Rate 3-D Vector Flow Imaging in the Frequency Domain**," Applied Sciences, vol. 10, no. 15, p. 5365, Aug. 2020, doi: 10.3390/app10155365.*

***S. Rossi**, F. Fool, A. Ramalli and P. Tortoli, "**Experimental Validation of a New Method for 3-D Vector Flow Imaging in the Frequency Domain**" in 2020 IEEE International Ultrasonics Symposium (IUS), Las Vegas, NV, USA, Sep. 2020, pp. 1–3, doi: 10.1109/IUS46767.2020.9251341.*

5.1 Introduction

The development of 3-D vector flow imaging (VFI) methods has so far stimulated increasing interest. The first 3-D vector studies were limited to the investigation of a single sample volume and exploited multibeam or multi-transducer approaches [17], [18], [45]. Extension of VFI to a full volume has been recently made possible by the introduction of bidimensional transducer arrays [46]–[48], [43], [49], [50]. The first attempts were based on either row–column-addressed arrays [51], [52] or full 2-D arrays [42] together with transverse oscillations, but they required long acquisition schemes, thus limiting the temporal resolution. More recently, methods exploiting HFR sequences have been developed; they have been based either on a combination of autocorrelation and a least-squares fitting approach [41], on a 3-D block matching procedure with a 3-D similarity function [44], or on particle image velocimetry [53]. However, the latter two methods required multiple heart cycles with electrocardiogram stitching to reconstruct the whole volume of interest. On the other hand, the autocorrelation-based method was characterized by a high computational load requiring more than 1 h to process one heartbeat, despite it being implemented on a powerful graphics processing unit (GPU).

Of course, when two or three components of the velocity vector have to be estimated, the computational efficiency of the used algorithm plays a fundamental role, as its complexity can become $O(N^2)$ or $O(N^3)$, respectively, with N the number of estimation points. In this chapter, an efficient 3-D HFR VFI method is proposed, inheriting the benefits of the previous 2-D VFI method, already discussed in paragraph 2.3 , by extending it to the third dimension. Specifically, the displacement estimation along the three dimensions is here obtained through two 2-D HFR VFI estimations on perpendicular planes.

5.2 Methods

5.2.1 High-Volume-Rate Imaging

The imaging method used in this work is based on the transmission (Tx) of unsteered plane waves from a 2-D probe and on parallel beamforming in reception (Rx). Since no compounding is applied, full volumes can be

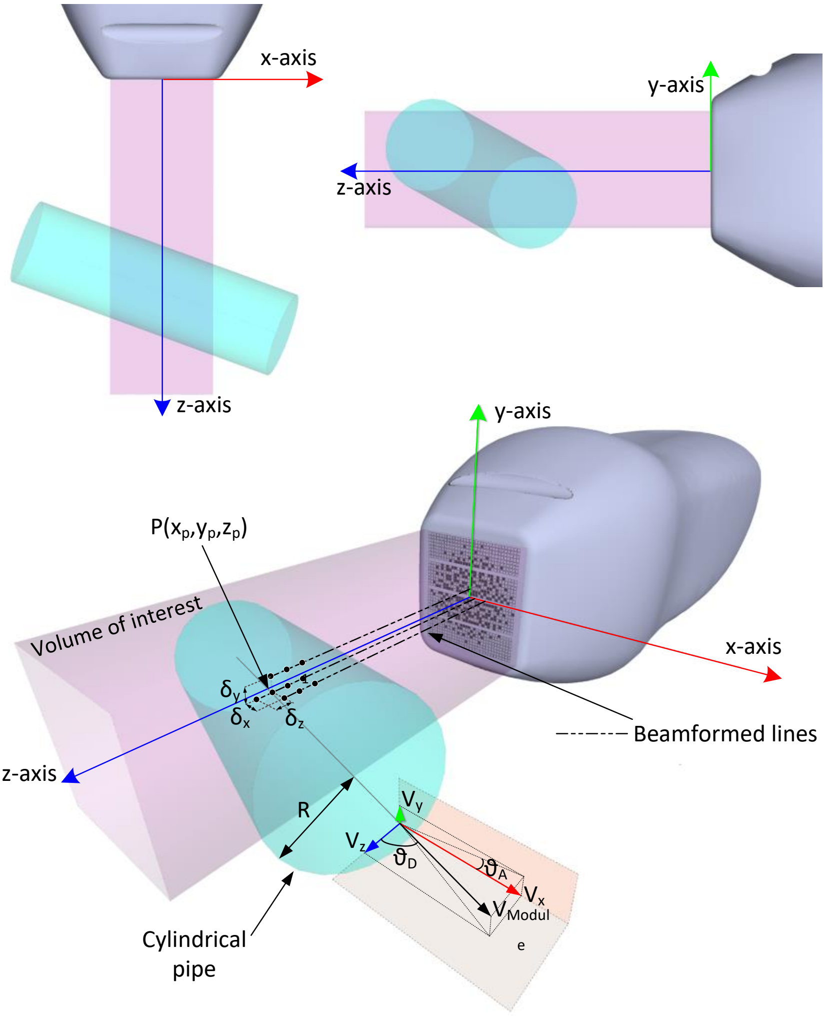

Fig. 5-1 Reference system for simulations and acquisitions. The volume of interest investigated by the 2-D plane wave is highlighted in light pink. The cylindrical pipe (light green) direction is defined by the beam-to-flow Doppler angle, ϑ_D, and the azimuth rotation angle, ϑ_A.

reconstructed at the maximum rate (i.e., equal to the pulse repetition frequency (PRF)). Then, radiofrequency (RF) volumetric data must be clutter-filtered to remove contributions due to stable or slowly moving tissues. Specifically, hereinafter, since only vessels with rigid walls are considered, clutter removal is obtained by a high-pass filter with a cutoff frequency of 5 Hz. Furthermore, RF echoes are sampled at frequency fs equal to 39 MHz; hence, the distance between pixels in the z direction is $\delta_z = c/(2fs) = 20$ µm. The lateral distance between pixels is the distance between beamformed lines (300 µm) both along the x direction (δ_x) and y direction (δ_y) (see Fig. 5-1).

5.2.2 3-D Displacement Estimation

In order to estimate the velocity components for a specific point of interest $P(x_p, y_p, z_p)$ (i.e., the black dot in Fig. 5-2), the volume of RF data is divided into parallelepipeds, hereinafter referred to as "kernels", containing $M_B \times N_B \times P_B$ pixels surrounding P. For each kernel, to estimate

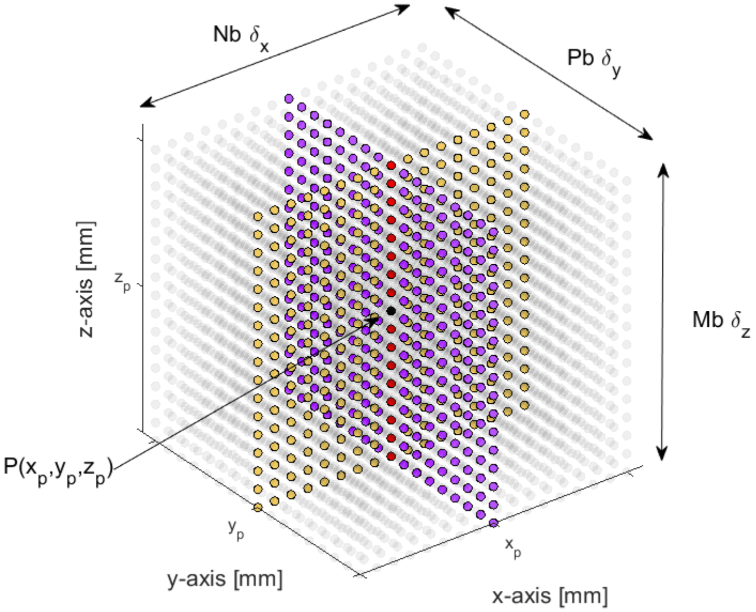

Fig. 5-2 Example of kernel region consisting of MB × NB × PB beamformed samples, distributed according to the step distances δz, δx, and δy for z, x, and y directions, respectively.

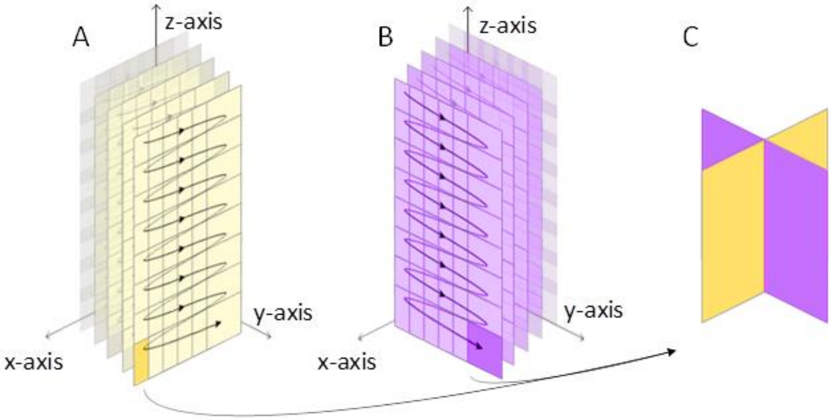

Fig. 5-3 3-D vector flow imaging (VFI) elaboration scheme. The beamformed volume samples are sequentially elaborated per plane in both directions (panels A and B). The corresponding components are finally grouped to obtain the velocity estimation (C).

the average displacement between consecutive Tx events, the 2-D VFI algorithm, described in paragraph 2.3 , is independently applied to the two perpendicular planes (yellow and purple in Fig. 5-2) that cross the kernel's vertical (red in Fig. 5-2) axis. Thus, the average (x, z) and (y, z) displacement components are obtained. Note that the displacement component along the z-axis is estimated twice, allowing a more robust assessment by averaging the two estimates. It is worth highlighting that kernels can be arbitrarily located (i.e., they can be either partially overlapped or isolated), only influencing the spatial resolution of vector velocity estimates. In this study, kernels were located on a regular grid and overlapped 80% and 90% in the axial and both lateral directions, respectively, thus giving the same spatial resolution of 0.3 mm along the three directions.

Given that the developed algorithm is highly parallelizable, in order to compute the 3-D displacement for the whole volume and to keep the computational burden as low as possible, the processing is split into three steps. First, the 2-D VFI algorithm is applied to the planes perpendicular to the y direction to compute both the (x, z) displacement components (Fig. 5-3A); then, the (y, z) components are similarly obtained by processing the data from planes perpendicular to the x direction (Fig. 5-3B); finally, the

TABLE 5.I

IMAGING, FLOW, AND PROCESSING PARAMETERS.

Imaging/Flow/Processing Parameters	**Value**
Central transmission (Tx) frequency (f_0)	3.7 *–7 ** MHz
Pulse repetition frequency (PRF)	500 Hz
Pixel step ($\delta_z \times \delta_x \times \delta_y$)	(0.02 × 0.3 × 0.3) mm
Beam-to-flow angles (ϑ_D, ϑ_A)	[(90,0),(85,0),(80,0), (90,45),(85,45),(80,45)]°
Barycenter depth (z_0)	16 mm
Peak velocity (v_{max}^{Ref})	7.5 cm/s
No. of frequencies$^{\$}$ (n_{fz} n_{fx})	[3, 10]
z-axis bandwidth (B_z)	0.74^{*} – 1.4^{**} MHz
Kernel size ($M_B \times N_B \times P_B$)	(1.5 × 2.5 × 2.5) mm

* Vermon probe ** Capacitive Micromachined Ultrasonic Transducer (CMUT) probe $ Refer to paragraph 2.3

velocity components corresponding to the same kernels are grouped (Fig. 5-3C). Here, this method was implemented using the basic Matlab functions and by exploiting only the central processing unit (CPU) of the host computer.

5.2.3 Simulations

Simulations were carried out in Matlab with Simag and Field II. As sketched in Fig. 5-1, a numeric phantom was developed to simulate a parabolic flow inside a straight, cylindrical vessel with 4 mm radius (R). Its axis was maintained at z_0 = 16 mm, while the beam-to-flow angle resulted from different combinations of ϑ_D and ϑ_A angles, as summarized in Table 5.I. The density of the randomly distributed scatterers was set at 27 scatterers per resolution cell. For each setup configuration, simulations were run to simulate a 1 s long acquisition (i.e., 500 consecutive RF data volumes were produced).

5.2.4 Experiments

In the experiments was used the same setup described on paragraph 4.2.2 and sketched on Fig. 4-3. The peak velocity was approximately set at 7.5 cm/s. The distance and the angle of the Vermon probe with respect to the pipe were set through a custom holder connected to the positioning system.

5.2.5 Performance Metrics

The performance metrics of the 3-D VFI method were evaluated in terms of relative bias ($\bar{B}_v$) and standard deviation ($\bar{\sigma}_v$) as proposed for the 2-D method, see paragraph 4.2.4 . Unlike the 2-D case, the points of interest for the error estimation were defined on a volume, instead on a surface, as $P(x_p, y_p, z_p)$ and they were located at distance shorter than 90% of pipe radius from the flow axis (refer to $R_{90\%}$ in Fig. 4-5). Therefore, the performances were evaluated for each of the three velocity components and module ($v_z, v_x, v_y, v_{Module}$), as follows:

$$\bar{B}_v = \frac{1}{v_{max}^{Ref}} \frac{1}{N_p} \sum_{p=1}^{N_p} \left(v^{Ref}(x_p, y_p, z_p) - \bar{v}(x_p, y_p, z_p) \right) \tag{5.1}$$

$$\bar{\sigma}_v = \frac{1}{v_{max}^{Ref}} \sqrt{\frac{1}{N_p} \sum_{p=1}^{N_p} \sigma_v(x_p, y_p, z_p)^2} \tag{5.2}$$

$$\sigma_v(x_p, y_p, z_p) = \sqrt{\frac{\sum_{u=1}^{N_F} \left(v(x_p, y_p, z_p, t_u) - \bar{v}(x_p, y_p, z_p) \right)^2}{(N_F - 1)}} \tag{5.3}$$

where the $v^{Ref}(x_p, y_p, z_p)$ is the reference parabolic profile with v_{max}^{Ref} = 7.5 cm/s of peak velocity.

5.3 Results

5.3.1 Simulations

Fig. 5-4 shows the three components and the module of the velocity profiles estimated along the z-axis by using the CMUT and Vermon probes. Six probe-to-flow orientations, distributed by columns, were chosen to test the method when (a) only one velocity component was nonzero (left column), (b) two velocity components were different from

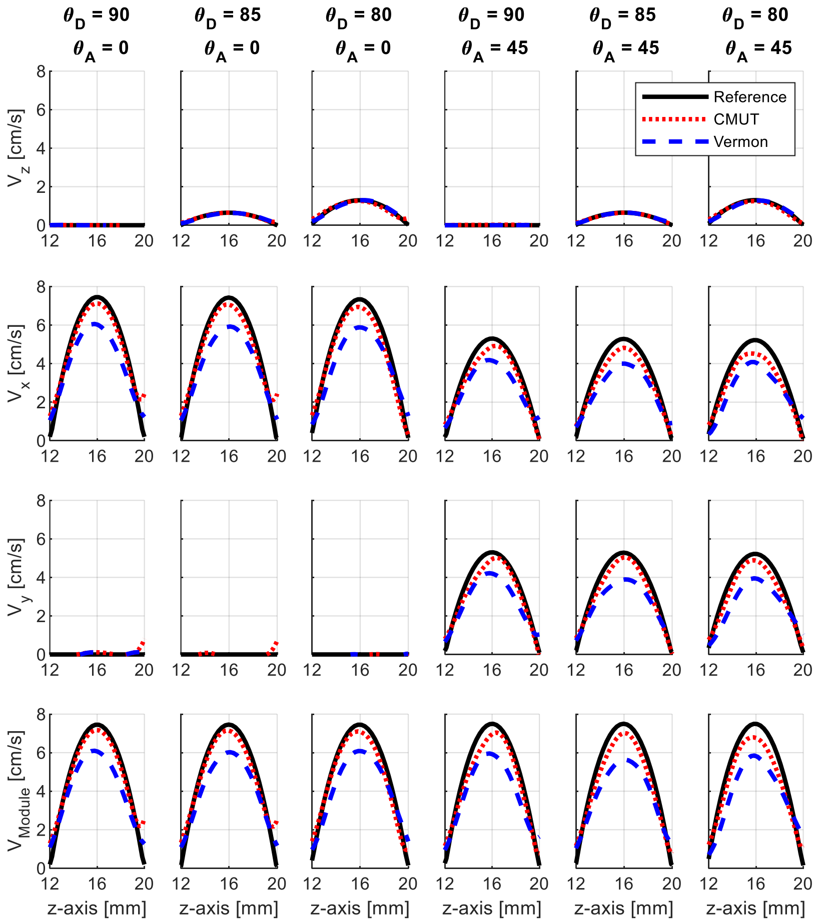

Fig. 5-4 Velocity profiles reconstructed along lines crossing the probe axis with different probe-to-flow orientations. The red dotted lines refer to the CMUT probe, the blue dashed ones to the Vermon probe. The black solid line is the reference velocity profile.

zero (columns 2–4), or (c) all three velocity components contributed to the velocity module (columns 5 and 6). In particular, the azimuth angle was set to 45° in the cases shown in the three rightmost columns, which implies that the lateral and elevation velocity components should be identical.

The differences between the profiles produced by the two probes can be appreciated in Fig. 5-4. The velocity components (v_x, v_y) were better estimated with the CMUT probe, the profiles of which more closely approached the reference. Similarly, the more pronounced underestimation of the lateral velocity components in the Vermon probe yielded a corresponding underestimation of v_{Module} (bottom panels). It is also worth noting that the estimated lateral velocity components (v_x and v_y, second and third rows) obtained for $\vartheta_A = 45°$ gave similar profiles, confirming their expected symmetry.

To visualize that the method behaved correctly even outside the axis of the probe, the 3-D representations of the flow distributions are shown in Fig. 5-5 for the CMUT probe and for $\vartheta_D = 90°$, $\vartheta_A = 0°$. Here, the surface view of the x–z plane for y = 0 is reported on the left and the y–z plane for x = 0 on the right.

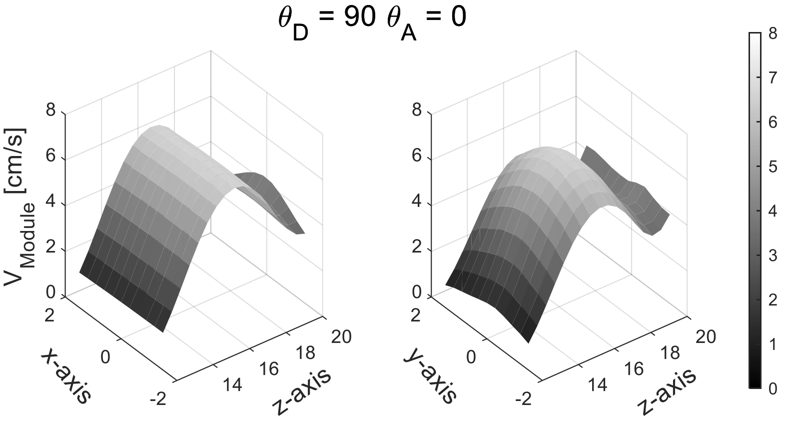

Fig. 5-5 Example of surface diagram for the CMUT probe simulation ($\vartheta_D = 90°$, $\vartheta_A = 0°$).

The relative bias, $\bar{B}_v$, and standard deviation, $\bar{\sigma}_v$, evaluated according to Equations (4.1)-(4.2) for all simulated conditions are reported in Table 5.II. For the CMUxzT probe, $\bar{B}_v$ and $\bar{\sigma}_v$ were always lower than 9.6% and 9.2%, respectively. On average, $\bar{B}_{v_{Module}}$ and $\bar{\sigma}_{v_{Module}}$ were 6.5% ± 6.4%, respectively. The results obtained with the Vermon probe, in general characterized by larger errors ($\bar{B}_{v_{Module}}$ and $\bar{\sigma}_{v_{Module}}$ resulted, on average, 14.4% ± 6.8%), were, however, less dependent on the beam-to-flow orientation, with a relative bias ranging (for the velocity module) between 12.6% and 16.3%.

TABLE 5.II

RELATIVE BIAS AND MEAN STANDARD DEVIATION FOR SIMULATIONS

CMUT Probe					
ϑ_D	ϑ_A	$\bar{B}_{v_z}$ $\pm\bar{\sigma}_{v_z}$[%]	$\bar{B}_{v_x}$ $\pm\bar{\sigma}_{v_x}$[%]	$\bar{B}_{v_y}$ $\pm\bar{\sigma}_{v_y}$[%]	$\bar{B}_{v_{Module}}$ $\pm\bar{\sigma}_{v_{Module}}$[%]
90°	0°	1.1 ±0.3	4.2 ±3.3	-1.4 ±8.3	3.6 ±3.3
85°	0°	1.1 ±0.3	5.7 ±4.1	-0.8 ±8.3	5.1 ±4.2
80°	0°	1.6 ±0.4	7.9 ±6.3	-1.1 ±8.7	7 ±6.1
90°	45°	1 ±0.3	4.7 ±6.5	3.6 ±6.5	5.6 ±7.5
85°	45°	1.2 ±0.3	6.6 ±7.2	5.3 ±7.2	7.8 ±7.9
80°	45°	1.9 ±0.4	8.5 ±8.9	6.6 ±8.7	9.6 ±9.2
Mean of $\bar{B}_{v_{Module}} \pm \bar{\sigma}_{v_{Module}}$ [%]					6.5 ±6.4
Vermon Probe					
ϑ_D	ϑ_A	$\bar{B}_{v_z}$ $\pm\bar{\sigma}_{v_z}$[%]	$\bar{B}_{v_x}$ $\pm\bar{\sigma}_{v_x}$[%]	$\bar{B}_{v_y}$ $\pm\bar{\sigma}_{v_y}$[%]	$\bar{B}_{v_{Module}}$ $\pm\bar{\sigma}_{v_{Module}}$[%]
90°	0°	0.7 ±0.9	14 ±4.4	-0.1 ±8.4	13.4 ±4.5
85°	0°	0.8 ±0.9	14.5 ±4.8	-0.1 ±8.7	13.7 ±5
80°	0°	1.3 ±0.9	14 ±5.7	-0.1 ±9.8	12.6 ±5.8
90°	45°	0.6 ±0.8	10.8 ±7	10.8 ±7.1	15.1 ±8.5
85°	45°	0.7 ±0.9	11.4 ±7	11.4 ±7	15.6 ±8.1
80°	45°	1.3 ±0.9	12.5 ±8.2	12.4 ±8.1	16.3 ±8.9
Mean of $\bar{B}_{v_{Module}} \pm \bar{\sigma}_{v_{Module}}$ [%]					14.4 ±6.8

5.3.2 Experiments

Particular care was taken to manually align the probe to the tube and obtain the same conditions used for simulation. However, from the analysis of the results, a slight misalignment of about 1° was noted in a couple of cases, which is within the accuracy of the position system. Hence, the actual angle (ϑ_D, ϑ_A) configurations were [(91,0), (85,0), (80,0), (91,44), (85,45), (81,43)]°.

Fig. 5-6 shows the velocity profiles experimentally obtained by using the Vermon probe. Qualitatively, the overall trend of the estimated profiles

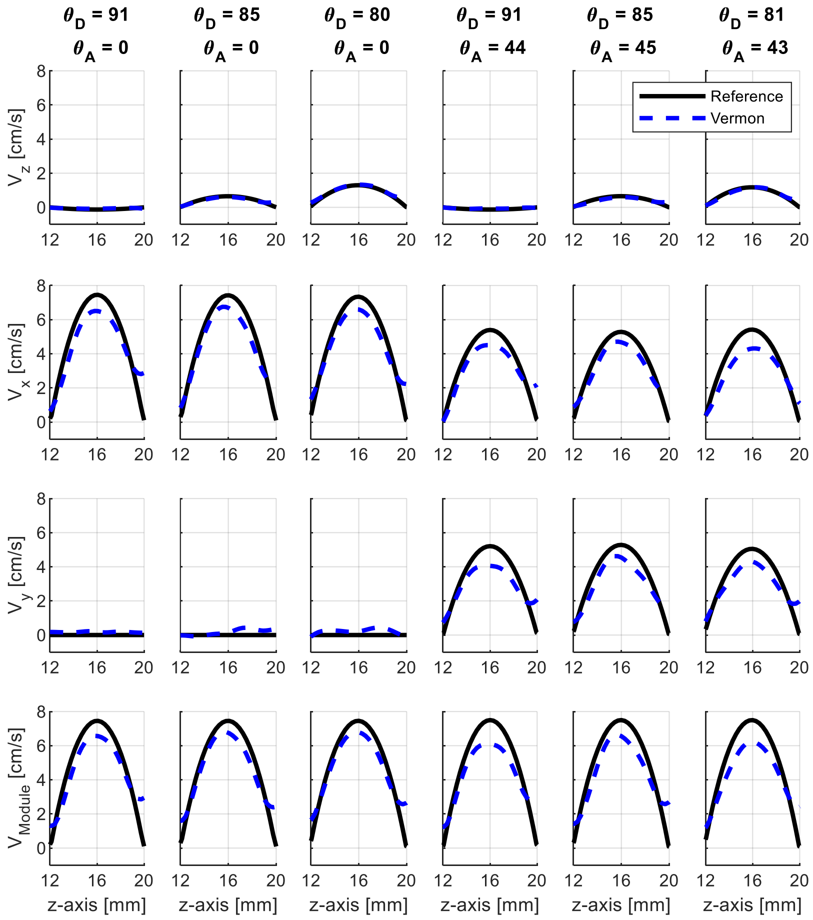

Fig. 5-6 Velocity profiles reconstructed by Vermon acquisitions, along the line crossing the probe axis with different probe-to-flow orientations. The black solid line is the reference velocity profile.

TABLE 5.III

RELATIVE BIAS AND MEAN STANDARD DEVIATION FOR EXPERIMENTS

Vermon Probe					
ϑ_D	ϑ_A	$\bar{B}_{v_z}$ $\pm\bar{\sigma}_{v_z}$[%]	$\bar{B}_{v_x}$ $\pm\bar{\sigma}_{v_x}$[%]	$\bar{B}_{v_y}$ $\pm\bar{\sigma}_{v_y}$[%]	$\bar{B}_{v_{Module}}$ $\pm\bar{\sigma}_{v_{Module}}$[%]
91°	0°	0.6 ±0.9	11 ±5.1	-2 ±8.9	10.2 ±5.2
85°	0°	1.1 ±1	10.5 ±6.2	-2 ±7.8	9.8 ±6.2
80°	0°	1.4 ±0.9	9.8 ±6.3	-2.7 ±9.2	8.8 ±6.3
91°	44°	0.6 ±0.9	9.3 ±7.8	10.1 ±7.5	13.3 ±9
85°	45°	1.3 ±0.8	8.7 ±6.8	9.6 ±7.1	12.6 ±7.7
81°	43°	1.9 ±0.9	11.4 ±8.4	10.5 ±7.9	14.6 ±9
Mean of $\bar{B}_{v_{Module}} \pm \bar{\sigma}_{v_{Module}}$ [%]					11.5 ±7.2

was the same observed from the simulations: v_z was estimated with good accuracy, while v_x and v_y suffered from higher underestimation. The errors reported in Table 5.III indicate that, on average, the relative error $\bar{B}_{v_{Module}}$ = 11.5% was lower (roughly 3%) compared with simulations, even if the standard deviation was slightly higher (7.2%). As highlighted by the plots and confirmed in Table 5.III, when ϑ_A = 45°, there was no mismatch between the estimates of the v_x and v_y components. The difference between the bias of the two velocity components was lower than 1%.

5.4 Discussion and Conclusion

A novel 3-D High Frame Rate Vector Flow Imaging method has been presented. The method is the extension of the 2-D HFR VFI. The proposed approach involves the transmission of unsteered plane waves from a bidimensional probe and parallel beamforming in reception. Then, the volume of beamformed data is divided into 3-D kernels and, for each of them, 3-D vector flow is estimated.

Simulations were performed for two 256–element spiral probes having comparable dimensions (~1 cm): the first one was based on a 1024-element piezoelectric probe manufactured by Vermon; the second one was based on a CMUT prototype that is currently under development [54]. These probes were chosen since they are illustrative of the performance achievable by the proposed method at different frequencies (3.7 and 7.0 MHz). Furthermore, it was possible to connect the Vermon probe to the ULA-OP 256 research scanner to perform experimental tests. Simulations and experiments were conducted at depths around 16 mm, which are compatible with both probes and with possible peripheral vascular applications. The performance was assessed, for different beam to flow angles, in terms of bias and standard deviation. Even if both experiments and simulations were conducted for a maximum flow speed of 7.5 cm/s - suggested by the limited entrance length of the experimental flow phantom - the PRF was accordingly set to a low value of 500 Hz so that, in the worst case ($\vartheta_D = 80°$ for high frequency CMUT probe), the produced Doppler shift along the z direction was about 50% the aliasing limit. Hence, the obtained results indicated that the possible proximity to the aliasing limit is not a crucial issue in the proposed method.

As reported in Table 5.II simulations have shown that the CMUT probe, in the presented cases, performed better than the Vermon one (mean bias ± standard deviation: 6.5% ± 6.4 vs 14.4 ± 6.8). This difference can be attributed to the characteristics of the two probes, i.e. similar equivalent apertures (~6 mm) and different central frequencies, which are known to give better spatial resolution for higher frequencies (CMUT) probes. In addition, the CMUT probe results are consistent with those (10 ± 5%) obtained for the 2-D method with a 6 MHz linear array probe [7] This is particularly remarkable considering the noticeable differences between the arrays used in the two cases, which involve elements of dimensions passing from 0.2×6 mm for the linear array, to about 0.3×0.3 mm for the 2-D arrays.

The performance of Vermon experimental results have confirmed that of simulation results, with a slightly better bias but a slightly higher standard deviation, which was probably due to the no-idealities of the measurement setup. In particular, the peristaltic pump introduced flow fluctuations that could not be sufficiently attenuated with the flow stabilization system. Even if a bigger pulsation dampener or a higher hydraulic resistance might have been used to limit the flow fluctuations, it is believed that the non-ideality of the experimental setting had a limited impact on the final results and did not affect their value.

The computational cost of the proposed method can be assessed by referring to the analysis carried out for the 2-D method [7]. Indeed, being the 3-D VFI the 2-step extension of the 2-D method, the overall computational cost remains of the order O(N). This is much lower than the 3-D cross-correlation based algorithms, natively $O(N^3)$, which may be decreased, through appropriate optimizations, to reach an order of complexity at least $O(N^2)$. Even if the proposed method was tested offline, i.e. by post-processing the acquired raw data, it is part of the “high-frame-rate” family, since one full (Doppler) frame can be obtained after each Tx event. Furthermore, the algorithm for 3-D VFI is highly parallelizable and is suited for the implementation on GPUs, as already shown for 2-D VFI in [37]. Main limitations of parallel computing are linked to data transfer rates and number of global memory accesses, which both need a proper and careful design of memory coalescing. Anyway, also considering the increasing computational power of GPU-based devices, in the near future, the implementation of 3-D VFI should be feasible in real-time, targeting input frame rates of at least 7 kHz, i.e. sufficient to estimate flow speeds up to 100 cm/s.

One of the main limitations of this work was using unsteered plane waves, which limited the extension of the investigated region due to the small size of the probe aperture. For example, as seen in in the right panel of Fig. 5-5, the paraboloid representative of the velocity module, was partially cut off, since only 3.6 mm (about one half of the pipe diameter) could be investigated along both the x and y axes. A possible alternative to extend the region of interest could be the transmission of diverging waves, although it should be taken into account that they involve a worse signal-to-noise ratio (SNR)[55], [56].

Finally, it has to be highlighted that, in this thesis, the novel method has been implemented by using sparse spiral arrays rather than full 2-D arrays [48], which allowed to perform the first experimental tests. However, it unavoidably involved a reduced SNR and a lower sensitivity to blood flow. This could be partially compensated by using coded imaging techniques [57] or in-probe pre-amplifiers. Likewise, doubling the number of active elements by exploiting two synchronized ULA-OP 256 systems [58], [59], could improve the system sensitivity and, at the same time, counteract the unavoidable grating lobes in the transmitted ultrasound beams associated to spiral arrays [56]. By taking these aspects into considerations, the results of this thesis appear extremely encouraging and confirm that sparse arrays may be a relatively cheap solution for the implementation of 3-D imaging on systems based on a limited number of channels.

Chapter 6. 2-D Vector Flow Imaging in Real-Time

This chapter presents a real-time system for high frame rate vector flow imaging, which estimates the displacements between consecutive radiofrequency frames from the corresponding phase shifts in the frequency domain.

The activity reported in this chapter resulted in the following paper:

***S. Rossi**, F. Acerbi, A. Dallai, F. Guidi, V. Meacci, A. Ramalli and P. Tortoli, "**Real-**Time System **for High Frame Rate Vector Flow Imaging**" in 2020 IEEE International Ultrasonics Symposium (IUS), Las Vegas,* NV, *USA,* Sep. *2020*, pp. 1–4, doi: 10.1109/IUS46767.2020.9251328.

6.1 Introduction

This chapter, with the aim of further reducing the computational load, proposes to process demodulated, down-sampled baseband (BB) data to relieve the hardware requirements, thus allowing a first real-time implementation of the 2-D vector flow imaging at HFR.

6.2 Methods

6.2.1 Vector Flow Imaging on Baseband Frames

As shown in Fig. 6-1, since the demodulation involves a shift of the spectrum from the transmission frequency f_0 to 0 Hz, two major changes had to be done to the RF-based VFI approach presented in paragraph 2.3 . First, the n_{f_z} frequencies of the DFT along the axial direction were still chosen on a bandwidth equal to $0.2 \times f_o$, but centered at 0 Hz. Then, equation (2.19) had to be updated, consider the frequency shift due to the demodulation, as follows:

$$\Delta_{zfm} = \frac{M_B}{2\pi(f_m + f_0)} \Delta\phi_{fm} \tag{6.1}$$

On the other hand, for the lateral displacement estimations, everything remains unchanged with respect to the RF-based approach.

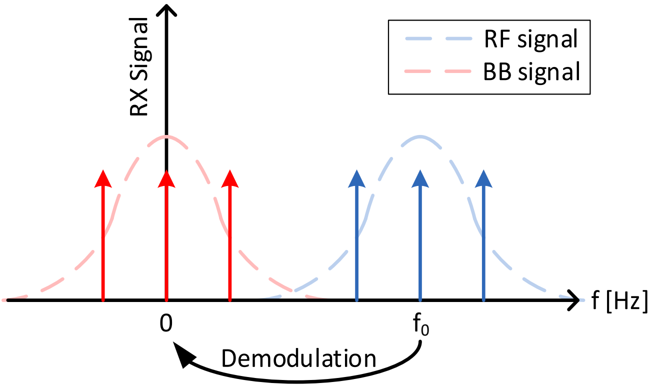

Fig. 6-1 Demodulation of RF signal to BB. The blue and red arrows represent the n_{fz} frequencies chosen for RF and BB algorithms, respectively.

6.2.2 Real-Time Implementation on the ULA-OP 256

The real-time processing flow of the research scanner ULA-OP 256 is shown in Fig. 6-2. Four Front End (FE) boards, each managing 32 independent channels, are used. In each board, RF data are beamformed through a delay and sum algorithm; then, they are quadrature demodulated by two multicore digital signal processors (DSPs). The BB data produced by the 4 FE boards are collected by the Master Control board (MC), on which the main DSP adds up the partially beamformed signals. The same DSP is also responsible for clutter filtering and BB-VFI processing. The clutter filter, Fig. 6-3, was implemented as a finite impulse response (FIR) high pass filter, which subtracts the average of the last N_{TAP} frames from the processed frame. The normalized frequency response, as function of the N_{TAP} was reported in Fig. 6-4.

This solution is computationally efficient, since it requires only two buffers, both having the size of one frame. The first buffer functions as an

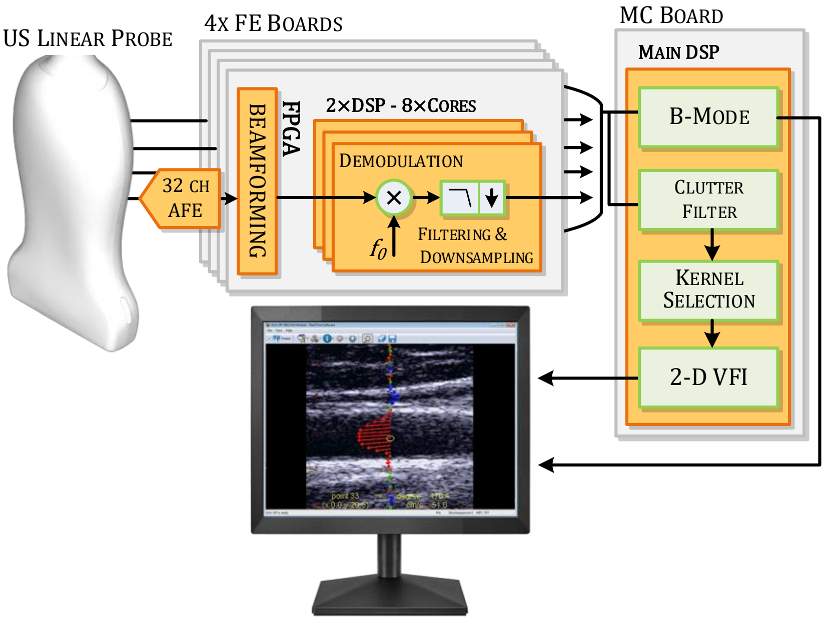

Fig. 6-2 Block diagram of the Rx chain of the ULA-OP 256 ultrasound scanner. The monitor on the bottom shows an example of visualization of the VFI 2-D method, which overlaps the velocity vectors on the B-Mode image.

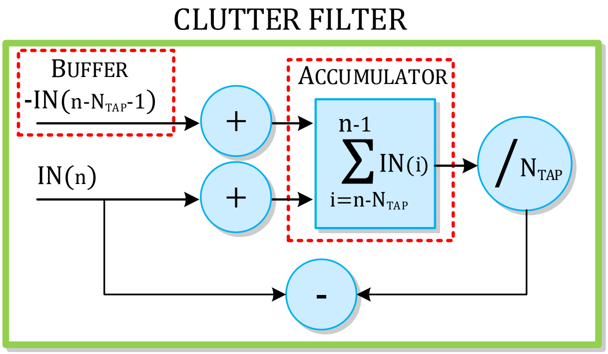

Fig. 6-3 Block diagram of the high pass filter applied before the 2-D VFI elaboration to attenuate the tissue clutter. The red dotted rectangles highlight the two buffers required.

accumulator for the moving average; the second buffer memorizes the (n-TAP-1)-th frame to be removed from the accumulator, Fig. 6-3.

To limit the computational cost, the number of estimation kernels per frame was parameterized, allowing the user to arbitrarily define their position over the region of interest. Every kernel is sequentially elaborated and, as soon as the processing of a frame is completed, the velocity estimates are directly sent to the PC for visualization.

It is worth highlighting that the main processing parameters (e.g. n_{f_z}, n_{f_x}, M_B, N_B, etc.) are user programmable.

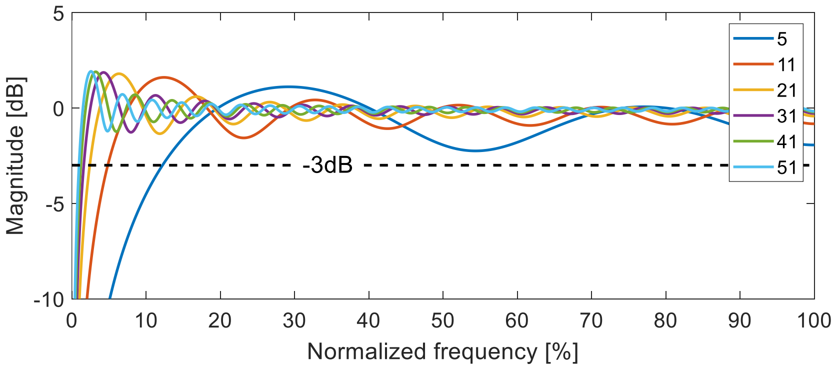

Fig. 6-4 Clutter filter frequency response by varying the N_{TAP}. The black dashed line represents the -3dB magnitude level.

6.2.3 Test Setup

As reported in Table 6.I, 128 elements of a linear probe (model LA533, Esaote S.p.A., Florence, Italy) were excited by 5-cycle sinusoidal bursts centered at f_0=6 MHz and weighted with a Hamming window. For each transmission (Tx) event, in reception (Rx), 64 central lines were beamformed, with a lateral step of δ_x=245 µm, coincident with the probe pitch. The method was tested on a steady laminar flow through Simag simulations and experiments with the ULA-OP 256. The main test parameters and method settings are summarized in Table 6.I. The BB down-sampling was set to 8, scaling the sampling frequency from 39.06 MHz RF to 4.88 MHz, which yields to δ_z=158 µm. Hence, in this case, considering a physical kernel size of 2.5×3.9 mm, M_B×N_B corresponded to 16×16 samples in z and x direction, respectively. However, it should be noted that the kernel is weighted by a 2-D Hann's window, which corresponds to an effective physical size of about 1.2×1.9 mm. N_{TAP} was set to 51, corresponding to a -3dB cut-off frequency of 0.5% of pulse repetition frequency (PRF).

TABLE 6.I

TEST PARAMETERS

System Parameters	
Tx Central Frequency (f_0) [MHz]	6
RF Rx Sampling Frequency [MHz]	39.06
BB Rx Sampling Frequency [MHz]	4.88
Number of Tx/Rx Elements	128
Beamformed Lines	64
Probe pitch [mm]	0.245
Blood Flow Parameters	
Inner Radius [cm]	4
Peak Velocity (v_p) [cm/s]	8
Scatterers Density in simulations [1/mm^3]	25
Method Settings	
No. of frequencies [n_{f_z}, n_{f_x}]	[3, 10]
Kernel-size [mm]	2.5 x 3.9

6.2.4 Performance Metrics

The accuracy of the BB VFI with respect to the RF version was assessed for both z and x components of the velocity. For each point P(x$_p$, z$_p$), located at a distance from the flow axis shorter than 0.9×R, the relative bias was calculated as:

$$\bar{B}_{v_z} = \frac{1}{v_{max}^{RF}} \frac{1}{N_p} \sum_{p=1}^{N_p} \left(v_z^{RF}(z_p, x_p) - v_z^{BB}(z_p, x_p) \right) \qquad (6.2)$$

where N_p is the number of selected points and $v_z^{RF}(z_p, x_p)$ and $v_z^{BB}(z_p, x_p)$ are the temporal means of the velocity components estimated with RF and BB respectively. The normalization factor v_{max}^{RF} is the maximum velocity of the RF VFI elaboration. The bias for the lateral component ($\bar{B}_{v_x}$) was similarly computed.

6.3 Results

6.3.1 BB-RF Results Comparison

The example in Fig. 6-5 shows that both the simulated and the experimental velocity profiles, obtained with RF and BB VFI, are similar, with a relative bias between 0.1% and 0.3% for the z and x velocity

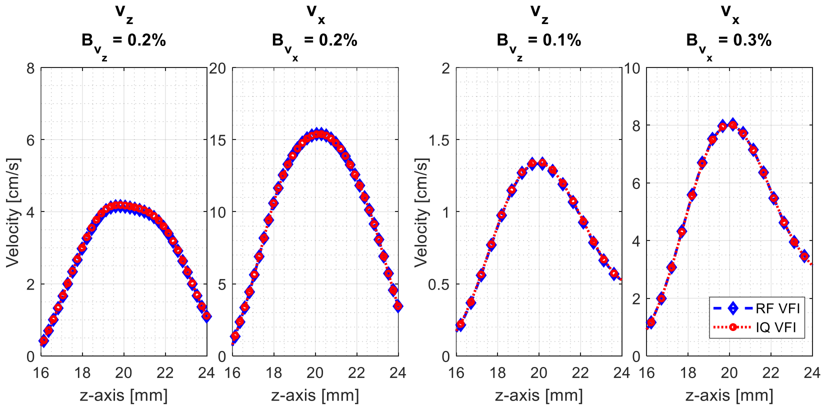

Fig. 6-5 Example of axial and lateral velocity components estimated with 2-D VFI based on RF and BB data. Left panels, simulations for ϑ_D=75° and PRF = 2500 Hz; right panels acquisitions for ϑ_D=80° and PRF = 500 Hz.

components, respectively. Overall, both approaches offer equivalent results both in simulation and acquisition with a relative bias always lower than 0.6%.

The computational cost of the two approaches was evaluated by considering the number of operations (sums and multiplications) needed for the estimation of the velocity components of one estimation kernel. As detailed in [7] for the RF VFI, computational cost was estimated by considering that the phase can be extracted from a look-up table and that the complexity of a sum and a multiplication can be considered equivalent on current DSPs. Fig. 6-6 shows the ratio between the computational cost of BB VFI and RF VFI with respect to the axial kernel size. For typical axial kernel size values, considering an eight-fold lower sampling frequency for BB data (see Table I), the ratio is always lower than 33%.

6.3.2 Real Time Performance

In order to assess the highest reachable PRF, the Rx chain has been preliminarily tested by activating the clutter filter but excluding the BB VFI. This processing module sustained the maximum transfer rate from the FE boards to the MC board, i.e. 38 mega sample per second, which, considering the settings in Table 6.I, corresponds to a maximum PRF of 4600 Hz.

Finally, the test on VFI processing, showed that the module can sustain up to 100k estimates per second. It corresponds to about 20 speed estimates at the maximum PRF of 4600 Hz.

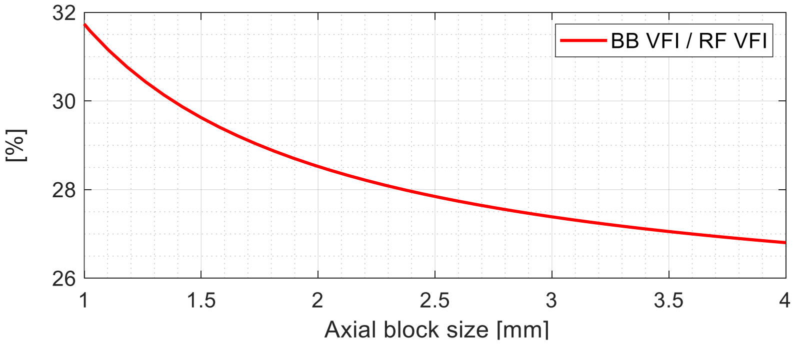

Fig. 6-6 Computational load ratio between the two approaches as a function of the axial kernel size, by introducing a subsampling of 8.

6.4 Discussion and Conclusion

In this chapter, a preliminary real-time implementation of the 2-D VFI method has been presented. Although the formerly proposed method based on RF data was highly efficient, compared to similar approaches, its computational cost was still high to be run in real-time on the ULA-OP 256. In particular, the on board DSP could not timely manage and process the high data rate of high frame-rate imaging. For this reason, further optimizations were developed and implemented. Here, differently from the original method, BB data have been processed to reduce (to about one third) the number of operations required to process each estimation kernel. Possible undesired effects on the accuracy of the proposed method were assessed. Both experiments and simulations have shown that passing from RF to BB processing, here does not involve significant accuracy loss.

Furthermore, a maximum PRF of 4600 Hz was achieved during real-time testing, producing 20 estimates for each frame. This result is encouraging considering that significant optimization of the DSP code is still possible. In addition, the multicore architecture of the MC’s DSP has not been exploited, yet. Parallelizing the processing on the 8 DSP cores should increase both the number of processed kernels and the achievable PRF, possibly sustaining up to 100k vector velocity estimates per second. Interesting improvements could also concern the automatic arrangement of the kernels within the image, for example through contour tracking algorithms [60], [61] capable of detecting the borders of the vessel, and by allowing the use of the so called Virtual Real Time modality, which was recently introduced in the ULA-OP 256 [62].

Chapter 7. Towards GPU Implementation on the ULA-OP 256

An efficient implementation of the 2-D VFI technique was developed by exploiting parallel computing and graphic processing units (GPUs). Based on these encouraging results, new hardware resources were added to the ULA-OP 256 by developing specific circuit boards and include GPUs to the signal processing chain.

The activity reported in this chapter resulted in the following publications:

***S. Rossi**, M. Lenge, A. Dallai, A. Ramalli, and E. Boni, "**Toward the Real Time Implementation of the 2-D Frequency-Domain Vector Doppler Method,**" in Applications in Electronics Pervading Industry, Environment and Society, vol. 573, S. Saponara and A. De Gloria, Eds. Cham: Springer International Publishing, 2019, pp. 129–135.*

***S. Rossi**, E. Boni, "**Embedded GPU Implementation for High-Performance Ultrasound Imaging**", Electronics, vol. 10, n. 8, Art. n. 8, gen. 2021, doi: 10.3390/electronics10080884.*

7.1 Introduction

Chapter 6 presented a preliminary real-time implementation of 2-D VFI on the ULA-OP 256, specifically on the DSP of the MC board. It allowed achieving up to 100k estimates per second, which, in some cases, could be a limiting factor to properly describe the dynamic and the spatial distribution of blood flows. Hence, in this chapter, to overcome such limitation, it is proposed to exploit the inherent parallelizability of the 2D-VFI algorithm for efficient parallel computing on graphic processing units (GPUs). A first implementation was done in CUDA on a PC equipped with a Nvidia GeForce GTX TITAN Black. Then, given the so encouraging processing performance, the hardware of the ULA-OP 256 was partially redesigned to accommodate new GPU resources.

7.2 Performance of 2-D VFI on GPU

7.2.1 Methods

Preliminary tests were conducted exploiting the Parallel Computing Toolbox supplied with Matlab to ease the implementation. The results were encouraging, as they presented a 5x speed-up factor for the GPU over the bare CPU implementation. This is reasonable, though not fully satisfactory, since the GPU Matlab toolbox does not allow the programmer to perfectly control every step of the workflow.

Consequently, a first version of the same algorithm was implemented in C++ using the CUDA toolkit (Nvidia Corporation, Santa Clara, CA, USA). The code cyclically transfers a set of fresh RF samples, comprising several frames, to the GPU, and arranges them in a buffer whose size is adjustable. At the same time, data processing is performed in parallel by thousands of cores of the device.

The performance tests were executed on a PC equipped with an Intel i5-2320 Processor (Intel Corporation, Santa Clara, CA, USA) and a GPU board Nvidia GeForce GTX TITAN Black, featuring 15 streaming multiprocessors, with 192 cores each (for a total of 2880 cores), and 6 GB of GDDR5 memory with very fast internal bus (up to 336 GB/s bandwidth).

TABLE 7.I

PROCESSING PARAMETERS.

Imaging/Flow/Processing Parameters	**Value**
No. of frequencies $[n_{f_z}, n_{f_x}]$	[(3-5), 10]
No. of Depths	1842
No. of Lines	64
M_B (Gates per Kernel)	150
OG (Ovelapping Gates on Consecutive Kernels)	110 (79%)
N_B (Lines per Kernel)	20
OL (Ovelapping Lines on Consecutive Kernels)	19 (95%)
M_w	42
N_w	45

The tests involved the execution of the optimized CPU Matlab code, the GPU Matlab code, and the GPU C++ code version. The performance of the different codes was assessed in terms of sustainable output frame rate, when processing previously stored RF frames obtained experimentally. The frame size and the most important computational parameters are shown in Table 7.I. The axial (M_w) and lateral (N_w) size of the output matrix, containing the velocity vectors, can be calculated as:

$$M_w = \frac{(Depths - M_B + 1)}{(M_B - OG)} \qquad N_w = \frac{(Lines - N_B + 1)}{(N_B - OL)} \tag{7.1}$$

where OG and OL are the numbers of overlapping gates and lines on consecutive blocks. The number of velocity estimations per frames equal $M_w \times N_w$.

7.2.2 Results

Fig. 7-1 (a) shows the performance of the three tested implementations in terms of frame rate. The sustainable output frame rate increases from about 320 frame/s, obtained with the GPU Matlab algorithm, up to almost 4500 frame/s, which corresponds to more than 8 million velocity estimations per second.

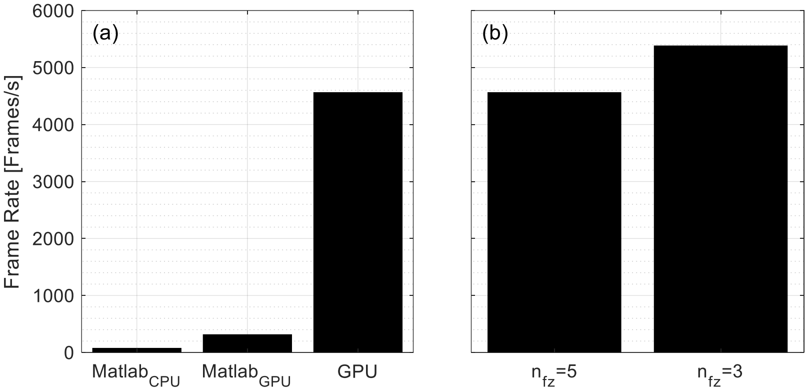

Fig. 7-1 Sustainable frame rates (a) for three different implantations with settings summarized in Table 7.I (with n_{fz}*=5) and incidence of the variation in the number of DFTz frequencies (b) on GPU(CUDA) implementation.*

Moreover, since, the size of the memory buffer, which is processed for each processing cycle, is crucial for the final real-time implementation, the number of processed frames per cycle was varied between 2 and 2000. The maximum efficiency of the algorithm was obtained for a buffer size of roughly 30 frames per cycle. Lastly, since also a reduction of the number of frequencies for the axial DFTs impacts on the performance, the sustainable frame rate was assessed for n_{f_z}=5 and n_{f_z}=3, as and suggested in [7]. Results in Fig. 7-1 (b) show that the frame rate can be increased up to 5380 frame/s, which corresponds to over 10M estimations per second.

7.3 Hardware Development

7.3.1 Development Overview

The modular architecture of the system described in paragraph 3.2 , is based on 8 Front-End (FE) boards, of 32 channel each. The FE boards are coordinated by a Master Control (MC) board connected to host PC though USB 3.0 or Ethernet (ETH). These boards are inter-connected through a Serial Rapid IO (SRIO) connection ring on a back-plane (BKP) board, which can reach a full duplex transfer rate of 10 GB/s for each FE board. The aim of this project was to introduce a new expansion board (EXP), hosting a GPU on board and allowing a fast communication with the host

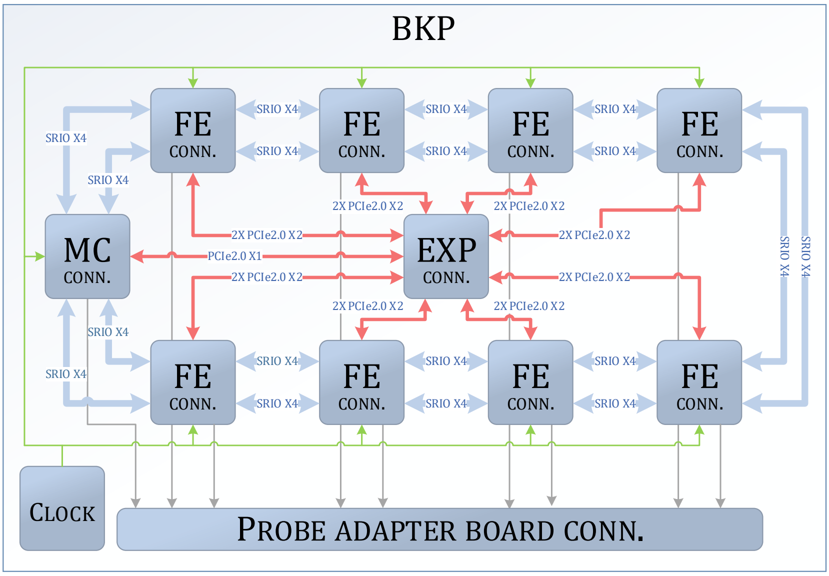

Fig. 7-2 The new Back-Plane v2.0 architecture of the ULA-OP 256. In light blue and red the SRIO and PCIe2.0 buses, respectively.

PC via a Peripheral Component Interconnect Express (PCIe) bus. This communication bus was chosen because the PCIe lanes of the DSPs on board, both on the FEs and on the MCs, had already been routed until the backplane connectors. The hardware development involved the design, from scratch, of the EXP board and the re-design of the BKP board. The latter, in particular, required to route all lanes of the PCIe in a star network, sketched in Fig. 7-2. This allowed connecting each FEs and the MC with a PCIe switch onboard the EXP that could also be connected the onboard GPU. These changes have been designed to ensure backward compatibility with the previous system configuration.

Communication Protocol: PCIe

The PCIe is a high-speed, serial bus standard for personal computer expansion, which is maintained and developed by the PCI-SIG (PCI Special Interest Group) community [63]. The PCIe bus is characterized by a full-duplex point-to-point topology. The peripheral devices, referred-to as End-Points (EPs), are connected to the host named Root Complex (RC) through switches, which perform the function of nodes. The connections

TABLE 7.II

PCIE THROUGHPUT SPECIFICATIONS.

PCIe Version	**Line Code**	**Transfer Rate** [giga transfers per second]	**Throughput [GB/s]**				
			×1	**×2**	**×4**	**×8**	**×16**
2.0	8b/10b	5.0	0.5	1	2	4	8
3.0	128b/130b	8.0	0.985	1.969	3.938	7.877	15.754

are made up of pairs of differential lines Tx and Rx, called lanes. The number of lanes per link could be from 1 to 32 (×1, ×2, ×4, ×8, ×12, ×16 and ×32) and is automatically negotiated during the initialization process. Moreover, the protocol does not provide limitations on simultaneous access between multiple EPs.

The PCIe versions implemented in this project are 2.0 and 3.0. PCIe 2.0 provides a throughput of 0.500 GB/s and a transfer rate of 2.5 giga transfer per second per line in each direction. The transfer rate is obtained considering the line encoding used, which in PCIe 2.0 is of type 8b / 10b corresponding to a 20% overhead. The PCIe 3.0 achieves a rate of 8 giga transfer per second by upgrading the encoding scheme to 128b/130b which reduces the overhead to 1.54% (2/130). The link performance of some PCIe configurations are reported in Table 7.II.

7.3.2 Back-Plane Board

As introduced in the previous paragraph, the BKP board houses the connections between all the ULA-OP 256 boards, according to the architecture sketched in Fig. 7-2. For each FEs and the MC there was two kinds of connector: one for analog and power signals, Fig. 7-3 (a) and another for high speed (HS) signals, Fig. 7-3 (b). The latter connectors, in addition to the SRIO lanes and the system clock distribution, were also exploited to connect, via PCIe, the different boards (FEs and MC) to the EXP board.

Specifically, for each DSP of the FE boards a PCIe 2.0 ×2 bus was routed, while for the single DSP on the MC board the bus was a PCIe 2.0 ×1, for a total of 66 differential lanes. These lanes were joined to the two HS connectors of the EXP board, positioned as shown on Fig. 7-3 (c). The routing was compliant with all constraints indicated by the protocol, taking care to minimize the stubs due to the through-hole connectors used. For this reason, compared to the previous version of the board, two additional

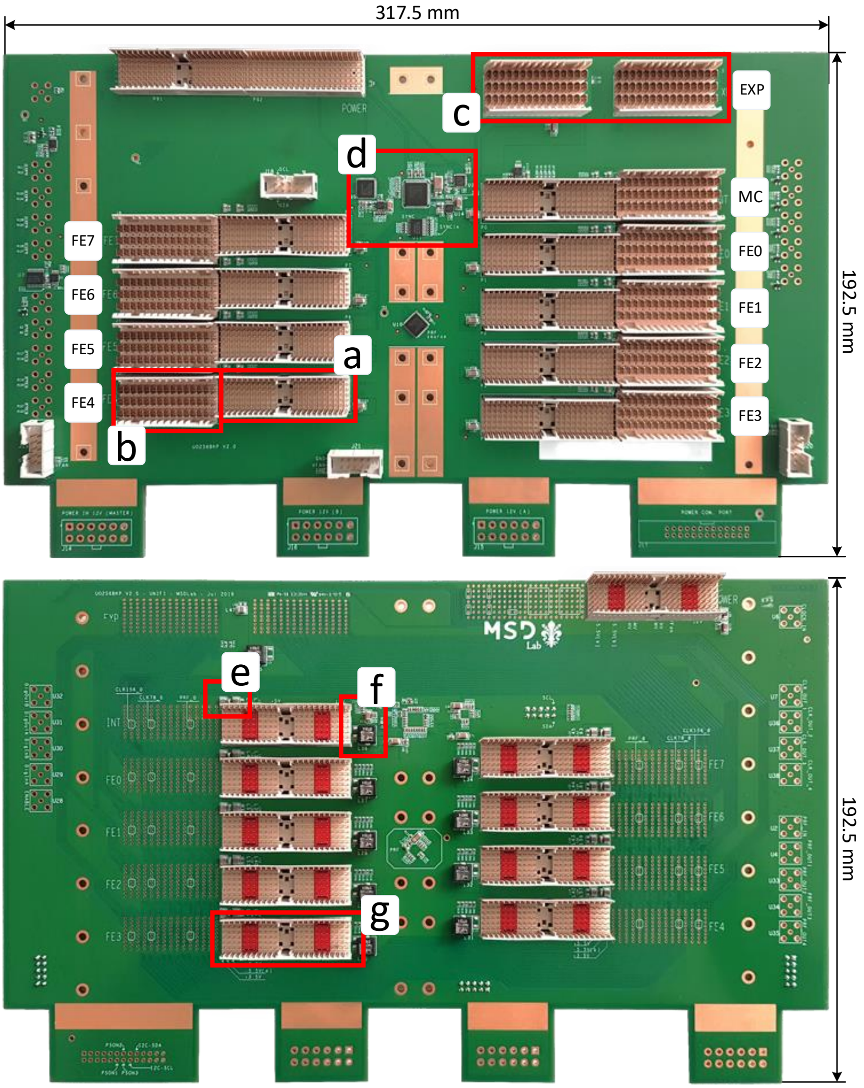

Fig. 7-3 Top and bottom views of the Back-Plane v2.0.

signal layers were introduced, which also allowed a more accurate routing of the SRIO, the system clock, and PRF lanes, to which an internal layer was dedicated. Fig. 7-3 (d) highlights the low jitter phase locked loop (PLL) buffer (AD9522-4, Analog Devices), which generates the system clock of 78.125 MHz.

In order to improve the stability of the FE power supplies and reduce the switching noise injected on analog channels, additional filtering stages were added, Fig. 7-3 (e-f). Also, the bottom side of the backplane hosts 9 connectors, which interface with the probe adapter board, including the actual probe connector, Fig. 7-3 (g).

7.3.3 Expansion Board

The expansion board was designed to increase storage capabilities, processing resources, and data throughput rates to external processing units. The block diagram with the main resources was shown in Fig. 7-4. The EXP was equipped with an M2 memory slot (Fig. 7-5 (a)), a Jetson AGX Xavier (NVIDIA, Santa Clara, CA, USA) [64] (Fig. 7-5 (b)) and an PCIe ×16 connector (Fig. 7-5 (c)). The M2 can host a common consumer SSD (solid state drive) NVMe (non-volatile storage memory express) storage with a capacity of up to 2 TB. The Jetson AGX Xavier is an

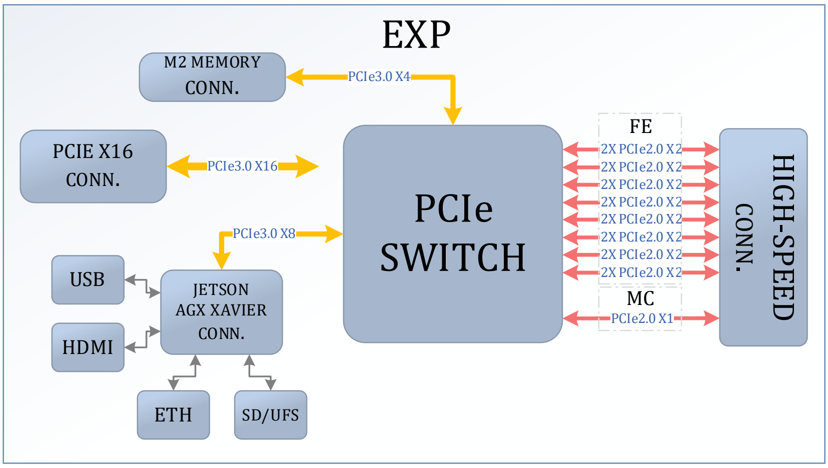

Fig. 7-4 PCIe connection diagram of Expansion board. In red and yellow the PCIe2.0 and PCIE3.0 bus, respectively.

embedded system-on-module (SOM) which integrates a 512-core Volta GPU controlled by an embedded operating system Linux that run on an Octal-core NVIDIA Carmel ARMv8.2 CPU. Also, the EXP mounts on board the Ethernet, USB, HDMI and SD/UFS Fig. 7-5 (d-e) connectors to independently control the Jetson module. Finally, the PCIe ×16 connector allows creating a high-speed channel via a jumper cable to an external PC motherboard or a custom daughterboard.

The core of the project is represented by the PCIe switch PEX8796 (Broadcom Limited, Irvine, CA, USA), Fig. 7-5 (f), capable of managing up to 96 lines PCIe3.0, distributed in 6 stations of 4 ports each (natively

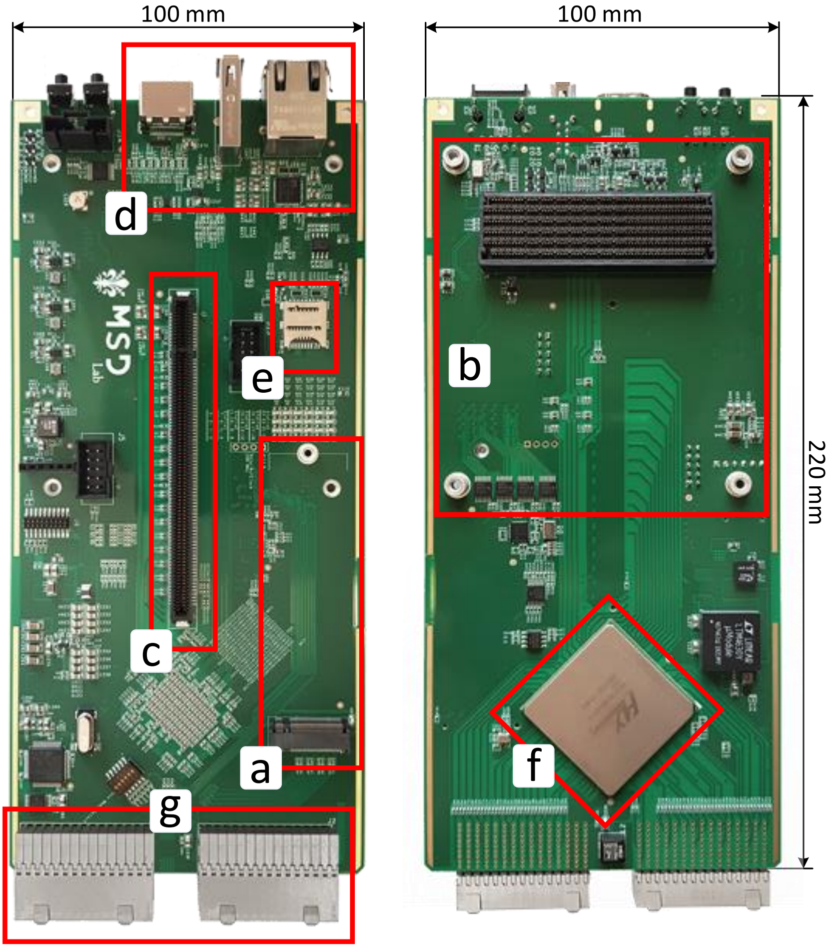

Fig. 7-5 Top and bottom views of the Expansion board.

×4). The ports of the same station can be combined to obtain configurations up to ×16. The device can interconnect ports configured with different numbers of lines and guarantees the backward compatibility with PCIe 2.0 standard. The diagram of the PCIe connections is highlighted on Fig. 7-4.

The system was designed to exploit all the available ports, configured as follows:

- 17 ports reserved to all the PCIe channels of DSPs integrated on the FE and MC boards (1 port for each DSP), linked via HS connectors Fig. 7-5 (g)
- 1 port (PCIe3.0 ×4) for the M2 memory slot
- 2 ports (PCIe3.0 ×8) for Jetson
- 4 ports (PCIe3.0 ×16) for the PCIe connector

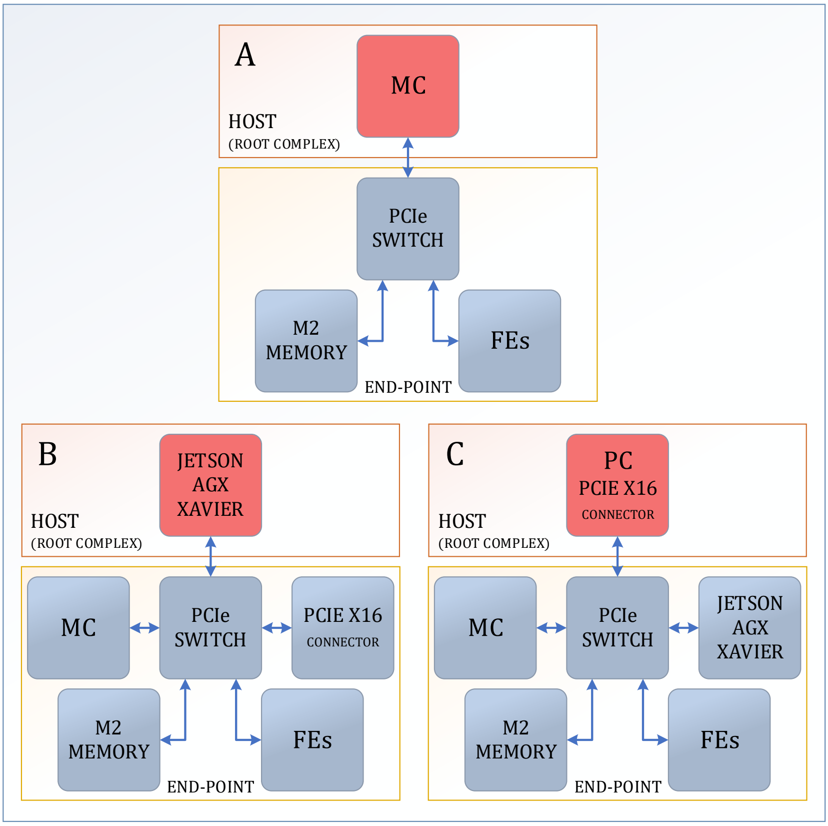

Fig. 7-6 The single host architecture with 3 different Root Complex (Host) scenarios.

Host Configurations

The architecture provides a single host configuration, with the possibility of setting the RC to be the MC DSP, the Jetson, or an external PC, Fig. 7-6. However, according to the PCIe protocol, as soon as the network is instantiated, any device can initiate a transaction with any other devices. It should be noted that it is not necessary for all resources to be always connected. The PCIe switch automatically detect which are disconnected, by isolating the corresponding ports from the network.

The simplest configuration, Fig. 7-6 (A), expands the interconnections between the FEs and the MC. This configuration is meant for those cases in which the use of GPU is not required. The most portable GPU based configuration of the system is represented in Fig. 7-6 (B). In this case, the PCIe ×16 connector can still be used to integrate additional PCIe external resources, such as expansion daughterboards for additional GPUs. To maximize the performance, at the expense of system portability, the configuration in Fig. 7-6 (C) can be adopted. A motherboard of a PC can be connected by the PCIe ×16 connector, which enables an almost unlimited amount of options to upgrade and increase the processing and storing resources, by using both commercial and customized devices.

7.3.4 Application Examples

As a first example of application, let's consider the external PC to be the host, Fig. 7-6 (C). Moreover, in order to facilitate the analysis, let’s assume that no processing operations (demodulation, filtering, beamforming, etc.) are carried out by the FPGAs and DSPs during the reception phase. Then, the raw data are directly transferred to the PC through the PCIe channel. As previously reported on Table 7.II, the maximum theoretical bandwidth of PCIe 3.0 ×16 is approximately 16

TABLE 7.III

PROCESSING PARAMETERS.

Imaging/Flow/Processing Parameters	Value
System Sample Frequency [MHz]	78.125
Sample Size [bit]	12

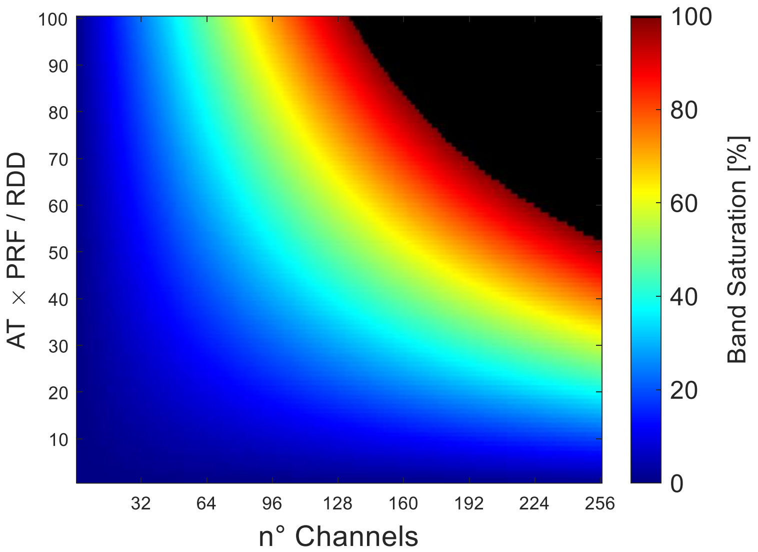

Fig. 7-7 Theoretical saturation level of PCIe 3.0 ×16 connection towards PC. The transfer band saturation percentage was color coded.

GB/s. Fig. 7-7 shows the color-coded image of the band saturation percentage, which is correlated with the number of active receiving channels, the PRF, the raw data decimation (RDD) and the acquisition time (AT), i.e. the sampling interval within two PRI event. For example, supposing to acquire from 256 channels, with a PRF of 10 kHz, a depth range of 35 mm, i.e. an acquisition time of 47µs, with an RDD of 1, the band saturation stands at 90%. Nevertheless, a PRF of 10 kHz, in theory, could allow a non-ambiguous range of 7.3 mm, requiring an acquisition time equal of 100µs. In this case, in order to acquire the whole range of depths, either the sampling frequency or the number of elements should be reduced. It is worth highlighting that the image in Fig. 7-7 highlights that halving the sampling frequency (RDD = 2) to 39 MHz is sufficient to theoretically obtain all the available depths without any limit on PRF and number of active channels.

As a second example of application, let's consider the Jetson to be the host, Fig. 7-6 (B). The Jetson AGX Xavier is connected via PCIe 3.0 × 8 bus, which compared to the previous example, provides half transfer bandwidth. As shown in Fig. 7-8 when considering the same settings of the

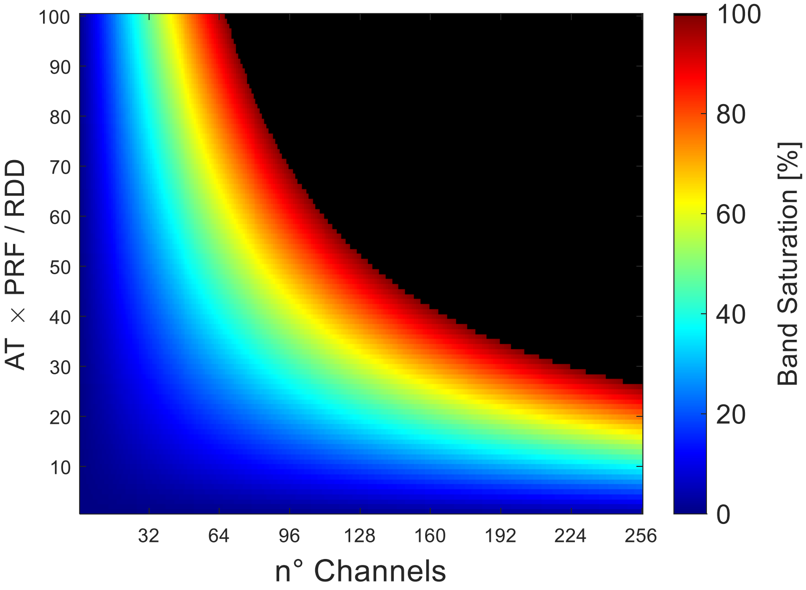

Fig. 7-8 Theoretical saturation level of PCIe 3.0 ×8 connection towards NVIDIA Jetson AGX Xavier. The transfer band saturation percentage was color coded.

previous example (PRF=10kHz, AT=47μs, n° channel=256), RDD = 2 is required to achieve a sustainable bandwidth occupation of 90%. However, this bandwidth represents a reasonable trade-off considering the limited resources of Jetson, compared to those of an expandable computer.

7.4 Conclusion

In this work, the implementation of the high frame rate 2-D vector blood flow imaging method in C++ (CUDA) language has been presented and its performance compared to that of a previous Matlab version. The new code was refined until the results were not substantially coincident with the results of the Matlab code.

The algorithm implementation in a GPU system has produced 4500 frame/s, thus capable of supporting a PRF of 4.5 kHz. Further tests were conducted on the dependence of the frame rate from the buffer size and by reducing the number of DFT frequencies, reaching up to 100 times the number of estimates achieved with the real-time implementation described in paragraph 6.3.2 .

Future improvements may be obtained by either a boosted optimization of the code and a revision of the method. Considering that the devices (CPU, GPU processors and motherboard) used in the tests do not represent the top level, the target goal of doubling such performance (9/10 kHz of PRF) may be considered achievable. Note that having such a high PRF is redundant for the needs of real-time display (for which frame rates of 50 Hz might be sufficient) but may be useful to enable further processing strategies addressed to improve the image quality and robustness of VFI estimates. Moreover, since the PRF is coincident with the Doppler signal sampling rate, high values are necessary for a correct analysis of high flow velocities.

Based on these encouraging results, new GPU hardware resources were added to the architecture of the ULA-OP 256. The project required the revision of the Back-Plane board by routing, in addition to the high-speed Serial Rapid IO ring bus, 66 PCIe differential lines to the high-speed connectors of a new Expansion board. The PCIe switch located on the expansion card allows interconnecting the ULA-OP 256 peripherals (Front-Ends and Master Control boards) and the NVMe SSD memory, both with an embedded Nvidia Jetson Xavier and with an external PC. This solution allows expanding the processing and storing capabilities of the system. The application example showed that, theoretically, the achievable transfer rates to a host PC could be high enough to transfer, in real-time, raw data acquired continuously with a sampling frequency of 39 MHz, otherwise compromises on the PRF, acquired depth range and number of channels should be made. Ultimately, this new system architecture, in addition to the 2-D VFI, may enable the real-time implementation of even more complex algorithms, e.g. 3-D VFI method.

Chapter 8. Conclusion

This chapter summarizes the contribution of the thesis and discusses possible directions for future research.

8.1 Summary of Contributions

This PhD project has aimed at providing methodological and technological contributions to the implementation of robust and reliable vector velocity measurements based on the transmission of PWs.

The topics explored in this Thesis can be summarized as follows:

- Preliminary experimental measurements and simulations have shown an increasing underestimation in the velocity measurements performed at increasing depths. Comparing the results based on the 2D-VFI method [7] with those obtained with the spectral Doppler approach, assumed as reference gold standard, it was verified that only part of the estimation error could be ascribed to the velocity estimation algorithm. It was hypothesized that the underestimation was related to the broadening of the transmitted beam on the elevation plane, associated to the focused acoustic lens present on linear array probes. Additional tests performed by replacing the focused lens with a flat (unfocused) lens, characterized by a more constant field width, confirmed the above hypothesis.
- A novel 3-D VFI method was proposed, capable of exploiting the benefits of the 2-D VFI version. The volume of beamformed RF samples, received by the transmission of PWs from a 2-D spiral array probe, was divided into kernels. The 3-D (x, y, z) displacement estimation was split in two separate 2-D VFI estimations applied to the two perpendicular planes, which cross the kernel axis. The method was tested with various probe-to-flow angles and validated both by simulation and experiments. This approach kept the complexity at O(N), which is much lower than that of other 3-D VFI approaches.
- Although the 2-D VFI method is characterized by a lower computational cost than other equivalent 2-D vector Doppler methods, it was not low enough for the real-time execution by the ULA-OP 256. In order to further reduce the computing load, it was proposed to process baseband data, instead of RF data, and to parametrize the number and position of estimation kernels. The proposed real-time implementation allowed processing up to 100k 2D velocity vector estimates per second.

- Preliminary tests of the 2-D VFI method implemented on GPUs, have shown a significant increase in performance, reaching up to 10M estimates per second. A revision of the ULA-OP 256 hardware was therefore evaluated, including an update of the backplane board and the design of a new expansion board. The scanner was thus connected to an external PC via a PCIe 3.0 ×16 bus while hosting on board an NVIDIA Jetson AGX Xavier. A preliminary estimation showed that the available transfer rate could be sufficient for the real-time implementation of more complex algorithms, including the new 3D VFI method proposed in this Thesis.

8.2 Direction of Future Work

Retracing the topics developed during this PhD project, multiple future perspectives can be summarized as follows:

- Development of specific probes and lenses to improve the accuracy of flow estimation methods over extended range of depths.
- The use of vessels’ lumen segmentation for an automatic positioning of the estimation kernels, which could be useful for the real-time implementation of 2-D VFI.
- Development and implementation of new real-time applications, at high frame rates, exploiting the new resources (GPUs) made available on the ULA-OP 256. An example could be 3-D VFI based on 256-element sparse array probes.
- Design and development of a new test phantom for experimental flow measurements.
- Design of a high-performance, custom, host PC to be adapted to the ULA-OP 256 rack, which could maximize PCIe transfer rates and system portability.

Bibliography

[1] D. H. Evans and W. N. McDicken, *Doppler Ultrasound: Physics, Instrumentation and Signal Processing*, 2nd Edition. Wiley-Blackwell, 1999.

[2] H. Ritchie and M. Roser, “Causes of Death,” *Our World Data*, Feb. 2018, Accessed: Sep. 03, 2020. [Online]. Available: https://ourworldindata.org/causes-of-death.

[3] J. A. Jensen, “FIELD: A Program for Simulating Ultrasound Systems,” *Med. Biol. Eng. Comput.*, vol. 34, no. Supplement 1, Part 1, Art. no. Supplement 1, Part 1, 1996.

[4] J. A. Jensen and N. B. Svendsen, “Calculation of pressure fields from arbitrarily shaped, apodized, and excited ultrasound transducers,” *IEEE Trans. Ultrason. Ferroelectr. Freq. Control*, vol. 39, no. 2, Art. no. 2, Mar. 1992, doi: 10.1109/58.139123.

[5] A. Ramalli, *Development of novel ultrasound techniques for imaging and elastography. From simulation to real-time implementation*, Premio Tesi di Dottorato. Firenze: Firenze University Press, 2013.

[6] E. Boni *et al.*, “Architecture of an Ultrasound System for Continuous Real-Time High Frame Rate Imaging,” *IEEE Trans. Ultrason. Ferroelectr. Freq. Control*, vol. 64, no. 9, pp. 1276–1284, Sep. 2017, doi: 10.1109/TUFFC.2017.2727980.

[7] M. Lenge, A. Ramalli, E. Boni, H. Liebgott, C. Cachard, and P. Tortoli, “High-frame-rate 2-D vector blood flow imaging in the frequency domain,” *IEEE Trans. Ultrason. Ferroelectr. Freq. Control*, vol. 61, no. 9, pp. 1504–1514, Sep. 2014, doi: 10.1109/TUFFC.2014.3064.

[8] A. Austeng and S. Holm, “Sparse 2-D arrays for 3-D phased array imaging - design methods,” *IEEE Trans. Ultrason. Ferroelectr. Freq. Control*, vol. 49, no. 8, pp. 1073–1086, Aug. 2002, doi: 10.1109/TUFFC.2002.1026019.

[9] M. Tanter and M. Fink, “Ultrafast imaging in biomedical ultrasound,” *IEEE Trans. Ultrason. Ferroelectr. Freq. Control*, vol. 61, no. 1, pp. 102–119, Jan. 2014, doi: 10.1109/TUFFC.2014.2882.

[10] P. Tortoli, G. Maines, and C. Atzeni, “Velocity Profile Reconstruction Using Ultrafast Spectral Analysis of Doppler Ultrasound,” *IEEE Trans. Sonics Ultrason.*, vol. 32, no. 4, pp. 555–561, Jul. 1985, doi: 10.1109/T-SU.1985.31630.

[11] P. Tortoli, F. Guidi, G. Guidi, and C. Atzeni, “Spectral velocity profiles for detailed ultrasound flow analysis,” *IEEE Trans. Ultrason. Ferroelectr. Freq. Control*, vol. 43, no. 4, pp. 654–659, Jul. 1996, doi: 10.1109/58.503727.

[12] P. Tortoli, G. Guidi, P. Berti, F. Guidi, and D. Righi, “An FFT-based flow profiler for high-resolution in vivo investigations,” *Ultrasound Med. Biol.*, vol. 23, no. 6, pp. 899–910, 1997, doi: 10.1016/S0301-5629(97)00017-3.

[13] J. A. Jensen, S. Nikolov, A. C. H. Yu, and D. Garcia, “Ultrasound Vector Flow Imaging: I: Sequential Systems,” *IEEE Trans. Ultrason. Ferroelectr. Freq. Control*, pp. 1–1, 2016, doi: 10.1109/TUFFC.2016.2600763.

[14] J. A. Jensen, S. I. Nikolov, A. C. H. Yu, and D. Garcia, “Ultrasound Vector Flow Imaging - Part II: Parallel Systems,” *IEEE Trans. Ultrason. Ferroelectr. Freq. Control*, vol. 63, no. 11, pp. 1722–1732, Nov. 2016, doi: 10.1109/TUFFC.2016.2598180.

[15] M. D. Fox, “Multiple crossed-beam ultrasound Doppler velocimetry,” *IEEE Trans. Sonics Ultrason.*, vol. 25, no. 5, pp. 281–286, Sep. 1978, doi: 10.1109/T-SU.1978.31028.

[16] B. Dunmire, K. W. Beach, K.-H. Labs, M. Plett, and D. E. Strandness Jr., “Cross-beam vector Doppler ultrasound for angle-independent velocity measurements,” *Ultrasound Med. Biol.*, vol. 26, no. 8, pp. 1213–1235, Oct. 2000, doi: 10.1016/S0301-5629(00)00287-8.

[17] O. Bonnefous, “Measurement of the complete (3D) velocity vector of blood flows,” in *IEEE 1988 Ultrasonics Symposium Proceedings.*, Oct. 1988, pp. 795–799 vol.2, doi: 10.1109/ULTSYM.1988.49487.

[18] V. L. Newhouse, K. S. Dickerson, D. Cathignol, and J.-Y. Chapelon, “Three-dimensional vector flow estimation using two transducers and spectral width,” *IEEE Trans. Ultrason. Ferroelectr. Freq. Control*, vol. 41, no. 1, pp. 90–95, Jan. 1994, doi: 10.1109/58.265826.

[19] P. Tortoli, G. Guidi, and P. Pignoli, “Transverse doppler spectral analysis for a correct interpretation of flow sonograms,” *Ultrasound Med. Biol.*, vol. 19, no. 2, pp. 115–121, Jan. 1993, doi: 10.1016/0301-5629(93)90003-7.

[20] P. Tortoli, A. Dallai, E. Boni, L. Francalanci, and S. Ricci, “An Automatic Angle Tracking Procedure for Feasible Vector Doppler Blood Velocity Measurements,” *Ultrasound Med. Biol.*, vol. 36, no. 3, pp. 488–496, Mar. 2010, doi: 10.1016/j.ultrasmedbio.2009.11.004.

[21] A. Marion, W. Aoudi, A. Basarab, P. Delachartre, and D. Vray, “Blood flow evaluation in high-frequency, 40MHz imaging: A comparative study of four vector velocity estimation methods,” *Ultrasonics*, vol. 50, no. 7, pp. 683–690, Jun. 2010, doi: 10.1016/j.ultras.2010.01.008.

[22] R. Steel, K. V. Ramnarine, F. Davidson, P. J. Fish, and P. R. Hoskins, “Angle-independent estimation of maximum velocity through stenoses using vector Doppler ultrasound,” *Ultrasound Med. Biol.*, vol. 29, no. 4, pp. 575–584, Apr. 2003, doi: 10.1016/S0301-5629(02)00736-6.

[23] L. N. Bohs, B. J. Geiman, M. E. Anderson, S. C. Gebhart, and G. E. Trahey, “Speckle tracking for multi-dimensional flow estimation,” *Ultrasonics*, vol. 38, no. 1–8, pp. 369–375, Mar. 2000.

[24] J. A. Jensen and P. Munk, “A new method for estimation of velocity vectors,” *IEEE Trans. Ultrason. Ferroelectr. Freq. Control*, vol. 45, no. 3, pp. 837–851, May 1998, doi: 10.1109/58.677749.

[25] M. J. Pihl and J. A. Jensen, “Measuring 3D velocity vectors using the Transverse Oscillation method,” in *2012 IEEE International Ultrasonics Symposium*, Oct. 2012, pp. 1881–1885, doi: 10.1109/ULTSYM.2012.0472.

[26] M. M. Pedersen *et al.*, “Comparison of Real-Time In Vivo Spectral and Vector Velocity Estimation,” *Ultrasound Med. Biol.*, vol. 38, no. 1, pp. 145–151, Jan. 2012, doi: 10.1016/j.ultrasmedbio.2011.10.003.

[27] S. Ricci, L. Bassi, and P. Tortoli, “Real-time vector velocity assessment through multigate Doppler and plane waves,” *IEEE Trans. Ultrason. Ferroelectr. Freq. Control*, vol. 61, no. 2, pp. 314–324, Feb. 2014, doi: 10.1109/TUFFC.2014.6722616.

[28] I. K. Ekroll, A. Swillens, P. Segers, T. Dahl, H. Torp, and L. Lovstakken, “Simultaneous quantification of flow and tissue velocities based on multi-angle plane wave imaging,” *IEEE Trans. Ultrason. Ferroelectr. Freq. Control*, vol. 60, no. 4, Art. no. 4, Apr. 2013, doi: 10.1109/TUFFC.2013.2621.

[29] J. Udesen, F. Gran, K. L. Hansen, J. A. Jensen, C. Thomsen, and M. B. Nielsen, “High frame-rate blood vector velocity imaging using plane waves: simulations and preliminary experiments,” *IEEE Trans. Ultrason. Ferroelectr. Freq. Control*, vol. 55, no. 8, Art. no. 8, Aug. 2008, doi: 10.1109/TUFFC.2008.858.

[30] J. Bercoff *et al.*, “Ultrafast compound doppler imaging: providing full blood flow characterization,” *IEEE Trans. Ultrason. Ferroelectr. Freq. Control*, vol. 58, no. 1, Art. no. 1, Jan. 2011, doi: 10.1109/TUFFC.2011.1780.

[31] S. Ricci, S. Diciotti, L. Francalanci, and P. Tortoli, “Accuracy and Reproducibility of a Novel Dual-Beam Vector Doppler Method,” *Ultrasound Med. Biol.*, vol. 35, no. 5, pp. 829–838, May 2009, doi: 10.1016/j.ultrasmedbio.2008.10.012.

[32] R. Steel and P. J. Fish, “Error propagation bounds in dual and triple beam vector Doppler ultrasound,” *IEEE Trans. Ultrason. Ferroelectr. Freq. Control*, vol. 49, no. 9, pp. 1222–1230, Sep. 2002, doi: 10.1109/TUFFC.2002.1041538.

[33] S. Ricci, A. Ramalli, L. Bassi, E. Boni, and P. Tortoli, “Real-Time Blood Velocity Vector Measurement Over a 2-D Region,” *IEEE Trans. Ultrason. Ferroelectr. Freq. Control*, vol. 65, no. 2, pp. 201–209, Feb. 2018, doi: 10.1109/TUFFC.2017.2781715.

[34] R. Steel and P. J. Fish, “Velocity bias and fluctuation in the standard dual beam Doppler reconstruction algorithm,” *IEEE Trans. Ultrason. Ferroelectr. Freq. Control*, vol. 49, no. 10, pp. 1375–1383, Oct. 2002, doi: 10.1109/TUFFC.2002.1041079.

[35] G. E. Trahey, J. W. Allison, and O. T. von Ramm, “Angle Independent Ultrasonic Detection of Blood Flow,” *IEEE Trans. Biomed. Eng.*, vol. BME-34, no. 12, pp. 965–967, Dec. 1987, doi: 10.1109/TBME.1987.325938.

[36] M. Lenge, A. Ramalli, P. Tortoli, C. Cachard, and H. Liebgott, “Plane-wave transverse oscillation for high-frame-rate 2-D vector flow imaging,” *IEEE Trans. Ultrason. Ferroelectr. Freq. Control*, vol. 62, no. 12, pp. 2126–2137, Dec. 2015, doi: 10.1109/TUFFC.2015.007320.

[37] S. Rossi, M. Lenge, A. Dallai, A. Ramalli, and E. Boni, “Toward the Real Time Implementation of the 2-D Frequency-Domain Vector Doppler Method,” 2019, pp. 129–135.

[38] L. Francalanci, “Sviluppo di applicazioni innovative per imaging Doppler ad ultrasuoni su un sistema ecografico di ricerca,” University of Florence, Firenze, 2010.

[39] P. Tortoli, R. S. Thompson, P. Berti, and F. Guidi, “Flow imaging with pulsed Doppler ultrasound and flow phantoms,” *IEEE Trans. Ultrason. Ferroelectr. Freq. Control*, vol. 46, no. 6, pp. 1591–1596, Nov. 1999, doi: 10.1109/58.808885.

[40] R. S. Thompson, G. Bambi, R. Steel, and P. Tortoli, “Intraluminal ultrasound intensity distribution and backscattered Doppler power,” *Ultrasound Med. Biol.*, vol. 30, no. 11, pp. 1485–1494, Nov. 2004, doi: 10.1016/j.ultrasmedbio.2004.09.001.

[41] M. Correia, J. Provost, M. Tanter, and M. Pernot, “4D ultrafast ultrasound flow imaging: in vivo quantification of arterial volumetric flow rate in a single heartbeat,” *Phys. Med. Biol.*, vol. 61, no. 23, p. L48, 2016, doi: 10.1088/0031-9155/61/23/L48.

[42] S. Holbek *et al.*, “Common Carotid Artery Flow Measured by 3-D Ultrasonic Vector Flow Imaging and Validated with Magnetic Resonance Imaging,” *Ultrasound Med. Biol.*, vol. 43, no. 10, pp. 2213–2220, Oct. 2017, doi: 10.1016/j.ultrasmedbio.2017.06.007.

[43] J. Provost *et al.*, “3D ultrafast ultrasound imaging in vivo,” *Phys. Med. Biol.*, vol. 59, no. 19, pp. L1–L13, Oct. 2014, doi: 10.1088/0031-9155/59/19/L1.

[44] M. S. Wigen *et al.*, “4-D Intracardiac Ultrasound Vector Flow Imaging–Feasibility and Comparison to Phase-Contrast MRI,” *IEEE Trans. Med. Imaging*, vol. 37, no. 12, pp. 2619–2629, Dec. 2018, doi: 10.1109/TMI.2018.2844552.

[45] G. Bruni *et al.*, “Measurement and Imaging of a Velocity Vector Field Based on a Three Transducers Doppler System,” in *Acoustical Imaging*, P. Tortoli and L. Masotti, Eds. Boston, MA: Springer US, 1996, pp. 431–437.

[46] A. Fenster, D. B. Downey, and H. N. Cardinal, “Three-dimensional ultrasound imaging,” *Phys. Med. Biol.*, vol. 46, no. 5, p. R67, May 2001, doi: 10.1088/0031-9155/46/5/201.

[47] E. D. Light, S. F. Idriss, P. D. Wolf, and S. W. Smith, “Real-time three-dimensional intracardiac echocardiography,” *Ultrasound Med. Biol.*, vol. 27, no. 9, pp. 1177–1183, Sep. 2001, doi: 10.1016/S0301-5629(01)00421-5.

[48] B. Diarra, M. Robini, P. Tortoli, C. Cachard, and H. Liebgott, “Design of Optimal 2-D Nongrid Sparse Arrays for Medical Ultrasound,” *IEEE Trans. Biomed. Eng.*, vol. 60, no. 11, pp. 3093–3102, Nov. 2013, doi: 10.1109/TBME.2013.2267742.

[49] M. F. Rasmussen, T. L. Christiansen, E. V. Thomsen, and J. A. Jensen, “3-D imaging using row-column-addressed arrays with integrated apodization - part i: apodization design and line element beamforming,” *IEEE Trans. Ultrason. Ferroelectr. Freq. Control*, vol. 62, no. 5, pp. 947–958, May 2015, doi: 10.1109/TUFFC.2014.006531.

[50] A. Ramalli, E. Boni, A. S. Savoia, and P. Tortoli, “Density-tapered spiral arrays for ultrasound 3-D imaging,” *IEEE Trans. Ultrason. Ferroelectr. Freq. Control*, vol. 62, no. 8, pp. 1580–1588, Aug. 2015, doi: 10.1109/TUFFC.2015.007035.

[51] M. Pappalardo *et al.*, “Bidimensional ultrasonic array for volumetric imaging,” WO2008083876A3, Sep. 25, 2008.

[52] S. Holbek, T. L. Christiansen, M. B. Stuart, C. Beers, E. V. Thomsen, and J. A. Jensen, “3-D Vector Flow Estimation With Row–Column-Addressed Arrays,” *IEEE Trans. Ultrason. Ferroelectr. Freq. Control*, vol. 63, no. 11, pp. 1799–1814, Nov. 2016, doi: 10.1109/TUFFC.2016.2582536.

[53] J. Voorneveld *et al.*, “4-D Echo-Particle Image Velocimetry in a Left Ventricular Phantom,” *Ultrasound Med. Biol.*, vol. 46, no. 3, pp. 805–817, Mar. 2020, doi: 10.1016/j.ultrasmedbio.2019.11.020.

[54] A. Stuart Savoia *et al.*, “A 256-Element Spiral CMUT Array with Integrated Analog Front End and Transmit Beamforming Circuits,” in *2018 IEEE International Ultrasonics Symposium (IUS)*, Kobe, Oct. 2018, pp. 206–212, doi: 10.1109/ULTSYM.2018.8579867.

[55] E. Roux, A. Ramalli, P. Tortoli, C. Cachard, M. C. Robini, and H. Liebgott, “2-D Ultrasound Sparse Arrays Multidepth Radiation Optimization Using Simulated Annealing and Spiral-Array Inspired Energy Functions,” *IEEE Trans. Ultrason. Ferroelectr. Freq. Control*, vol. 63, no. 12, pp. 2138–2149, Dec. 2016, doi: 10.1109/TUFFC.2016.2602242.

[56] E. Roux, F. Varray, L. Petrusca, C. Cachard, P. Tortoli, and H. Liebgott, “Experimental 3-D Ultrasound Imaging with 2-D Sparse Arrays using Focused and Diverging Waves,” *Sci. Rep.*, vol. 8, no. 1, Art. no. 1, Jun. 2018, doi: 10.1038/s41598-018-27490-2.

[57] A. Ramalli, E. Boni, A. Dallai, F. Guidi, S. Ricci, and P. Tortoli, “Coded Spectral Doppler Imaging: From Simulation to Real-Time Processing,” *IEEE Trans. Ultrason. Ferroelectr. Freq. Control*, vol. 63, no. 11, Art. no. 11, Nov. 2016, doi: 10.1109/TUFFC.2016.2573720.

[58] A. Ramalli *et al.*, “High-Frame-Rate Tri-Plane Echocardiography With Spiral Arrays: From Simulation to Real-Time Implementation,” *IEEE Trans. Ultrason. Ferroelectr. Freq. Control*, vol. 67, no. 1, pp. 57–69, Jan. 2020, doi: 10.1109/TUFFC.2019.2940289.

[59] S. Harput *et al.*, “3-D Super-Resolution Ultrasound Imaging With a 2-D Sparse Array,” *IEEE Trans. Ultrason. Ferroelectr. Freq. Control*, vol. 67, no. 2, pp. 269–277, Feb. 2020, doi: 10.1109/TUFFC.2019.2943646.

[60] M. Demi, M. Paterni, and A. Benassi, “The First Absolute Central Moment in Low-Level Image Processing,” *Comput. Vis. Image Underst.*, vol. 80, no. 1, pp. 57–87, Oct. 2000, doi: 10.1006/cviu.2000.0861.

[61] V. Gemignani, M. Paterni, A. Benassi, and M. Demi, “Real time contour tracking with a new edge detector,” *Real-Time Imaging*, vol. 10, no. 2, pp. 103–116, Apr. 2004, doi: 10.1016/j.rti.2004.02.005.

[62] C. Giangrossi *et al.*, “Virtual Real-Time for high PRF Multi Line Vector Doppler on ULA-OP 256,” *IEEE Trans. Ultrason. Ferroelectr. Freq. Control*, pp. 1–1, 2020, doi: 10.1109/TUFFC.2020.3017940.

[63] PCI-SIG, “PCI-SIG.” https://pcisig.com/.

[64] NVIDIA, “NVIDIA Jetson AGX Xavier,” *NVIDIA*. https://www.nvidia.com/it-it/autonomous-machines/embedded-systems/jetson-agx-xavier/.